

3DReact: Geometric deep learning for chemical reactions

Puck van Gerwen,^{†,‡,§} Ksenia R. Briling,^{†,§} Charlotte Bunne,^{‡,¶} Vignesh Ram
Somnath,^{‡,¶} Ruben Laplaza,^{†,‡} Andreas Krause,^{‡,¶} and Clemence Corminboeuf^{*,†,‡}

[†]*Laboratory for Computational Molecular Design, Institute of Chemical Sciences and
Engineering, École Polytechnique Fédérale de Lausanne, 1015 Lausanne, Switzerland*

[‡]*National Center for Competence in Research – Catalysis (NCCR-Catalysis), École
Polytechnique Fédérale de Lausanne, 1015 Lausanne, Switzerland*

[¶]*Learning & Adaptive Systems Group, Department of Computer Science, ETH Zurich,
8092 Zurich, Switzerland*

[§]*These authors contributed equally to this work.*

E-mail: clemence.corminboeuf@epfl.ch

Abstract

Geometric deep learning models, which incorporate the relevant molecular symmetries within the neural network architecture, have considerably improved the accuracy and data efficiency of predictions of molecular properties. Building on this success, we introduce 3DREACT, a geometric deep learning model to predict reaction properties from three-dimensional structures of reactants and products. We demonstrate that the invariant version of the model is sufficient for existing reaction datasets. We illustrate its competitive performance on the prediction of activation barriers on the GDB7-22-TS, Cyclo-23-TS and Proparg-21-TS datasets in different atom-mapping regimes. We show that, compared to existing models for reaction property prediction, 3DREACT

offers a flexible framework that exploits atom-mapping information, if available, as well as geometries of reactants and products (in an invariant or equivariant fashion). Accordingly, it performs systematically well across different datasets, atom-mapping regimes, as well as both interpolation and extrapolation tasks.

1 Introduction

Physics-inspired representations that take as input the three-dimensional structure¹⁻¹³ (as well as, in some cases, electronic structure¹⁴⁻¹⁷) of molecules and transform it into a fixed-length vector, while respecting known physical laws, have a rich history in molecular property prediction.^{1-10,12,13,18-30} Common desiderata³¹⁻³⁴ for high-performing representations are (i) smoothness, (ii) encoding of the appropriate symmetries to permutations, rotations and translations,^{24,35} (iii) completeness and (iv) additivity to allow for extrapolation to larger systems. Such fingerprints,^{2-8,11-13,24} being rooted in fundamental principles, are designed to be property-independent: a single representation can be constructed for a molecule to predict any quantum-chemical target. This is analogous to the molecular Hamiltonian, which specifies the energy and all other properties of a system as a function of atoms' types and positions in three-dimensional space (assuming the molecules are charge neutral and singlets). These representations are typically used in combination with kernel models due to their data efficiency, ability to deal with high-dimensional feature vectors, and interpretability of the similarity kernel.^{2-10,12,13,31-33} Early works showed that combining such representations^{2,4,6,8,36} with simple feed-forward neural networks instead of kernel models did not necessarily led to better performance.^{37,38}

More recently, end-to-end neural networks have been proposed that learn the representation as part of the (supervised) training process,³⁹⁻⁶¹ based on similar principles to the aforementioned physics-inspired representations: they take as input a three-dimensional structure, as well as in some cases charge and spin information.^{46,51-53} The network may be *invariant* or *equivariant* to rotations and translations of the input molecules. The for-

mer is typically achieved by operating on distances between atoms,^{39,40,42} and the latter by operating on relative position vectors and angular information processed by rotationally-equivariant convolutional layers.^{41,43–46,48–50,54–59,62} Equivariant models are naturally suited to predict vectorial^{43–45,48,49,59,62} or higher order tensorial^{52,54,55,59,63} properties. They have also been demonstrated to exhibit improved data efficiency and generalization capabilities compared to their invariant counterparts on predictions of scalar properties,⁴³ albeit at a higher computational cost. Nevertheless, given an expressive enough architecture (*i.e.*, using higher-order messages^{41,56,62,64–67} and/or enough convolutional layers^{43,52,56}), invariant models are sufficient for many property prediction tasks.⁵⁶

Despite these advances for molecular property prediction, the prediction of computed *reaction properties* (principally, reaction barriers^{36,38,68–82}) is still in its infancy.⁸³ Machine learning approaches span from utilizing simple two-dimensional fingerprints of reaction components^{84,85} (reactants and products) to physical-organic descriptors,^{75,76,80,82,86–98} or electronic structure-inspired features,⁹⁹ to transformer models^{100,101} adapted for regression,¹⁰² and 2D graph-based approaches.^{70,71,81,103} The latter, particularly the CHEMPROP model,^{71,103} are often best-in-class in predicting reaction properties.¹⁰³ It has been shown³⁸ that these models achieve their impressive performance by exploiting atom-mapping information,^{104–107} which provide information analogous to the reaction mechanism.

Another category of reaction fingerprints arises from discretization of physically-inspired functions^{2–10,12,13} constructed using a cheap estimate of the transition state (TS) structure⁷³ or rather the structures of the reaction components^{36,69,74}. The SLATM_d representation^{36,69} in particular has been shown³⁸ to yield accurate predictions of reaction barriers, particularly for datasets^{69,108} relying on subtle changes in the geometry of reactants and/or products. End-to-end models based on three-dimensional structures of reactants and products have also recently emerged.^{72,99,109} In a different vein, several works^{110–115} aim to directly predict the TS structure, which together with the reactant structure gives the reaction barrier. These approaches lie outside the scope of the property-prediction focus here.

Due to the diversity of challenges posed by different reaction datasets, neither atom-mapping-based models nor 3D-geometry-based models achieve consistently better performance on reaction property prediction tasks.³⁸ To date, no model has been proposed that can incorporate both chemical (atom-maps) and physical (geometry) priors. To address this gap, we introduce 3DREACT, a geometric deep learning model that encodes both the three-dimensional structures of reactants and products as well as atom-mapping information or proxies thereof to predict properties of chemical reactions (showcased here for activation energies).

We demonstrate the performance of 3DREACT on three datasets of reaction barriers: GDB7-22-TS,¹¹⁶ Cyclo-23-TS,¹¹⁷ and Proparg-21-TS.^{69,108} As discussed in previous works,³⁸ these datasets present a myriad of challenges for ML models, from the dependence on chemical information¹¹⁶ to the distinction of subtle changes in configurations.^{69,108} We show that, compared to state-of-the-art models for reaction property prediction,^{36,103} 3DREACT offers accurate and reliable performance across different datasets as well as atom-mapping regimes, reduced dependence on the quality of three-dimensional geometries, and stable extrapolation behavior.

2 Architecture

3DREACT is built from $O(3)$ -equivariant convolutional networks over point clouds as implemented in `e3nn`.¹¹⁸ Specifically, we use the tensor field network architecture⁴⁷ for molecular components as in Corso *et al.*¹¹⁹ While the architecture is equivariant by default, it can easily be made invariant (*vide infra*). The geometries of molecules constituting reactants and products of each reaction are passed through separate channels, detailed in Section 2.1. They are then combined to eventually predict a reaction property, such as the activation energy, as detailed in Section 2.2. The overall architecture is summarized in Figure 1.

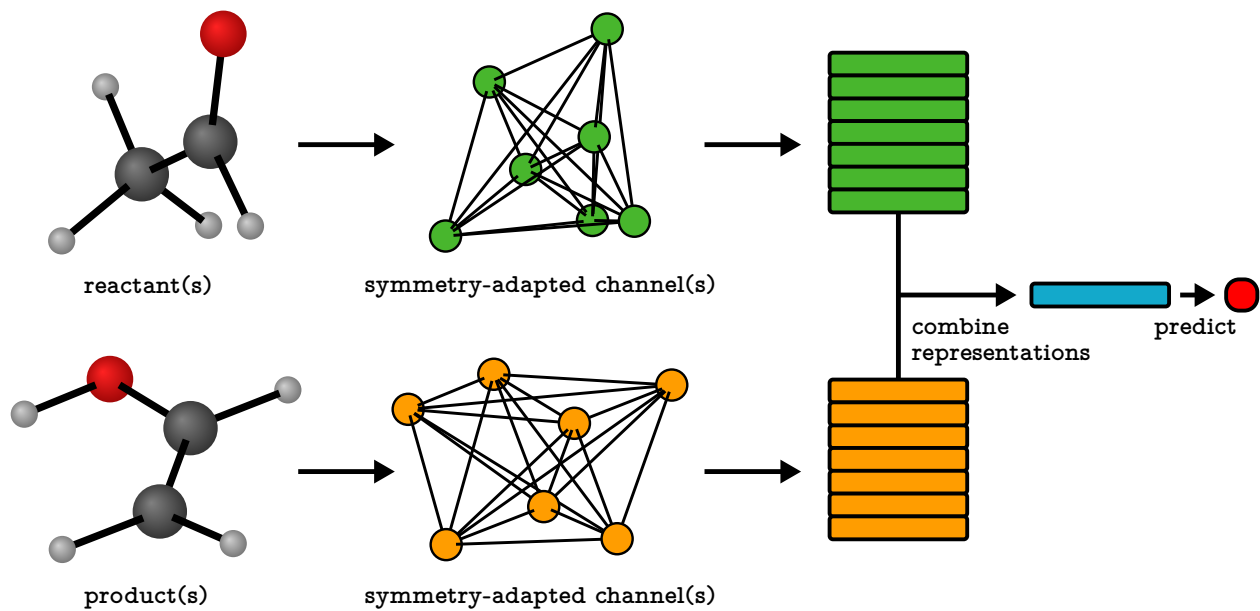


Figure 1: Architecture of 3DREACT. Molecules pass through independent symmetry-adapted (invariant or equivariant) channels (green and orange). These are combined to yield a reaction representation (blue) which is used to predict a reaction property, such as the activation energy (red dot).

2.1 Symmetry-adapted molecular channels

A molecule with N_{at} atoms is represented as a distance-based graph where nodes describe atoms and edges describe bonds. Instead of explicitly using connectivity information, the “bonds” of atom a are formed with all the neighboring $\text{Neigh}(a)$ atoms within the cutoff r_{max} . Initial scalar bond (edge) features $\{\mathbf{e}_{ab}^{(0)}\}$ between atoms a and b , as well as spherical harmonics filters $\{\mathbf{z}_{ab}\}$, are computed from internal coordinates, as detailed in equations S1–S4. The atom (node) features $\{\mathbf{x}_a^{(0)}\}$ are initialized with $n_f=16$ cheminformatics descriptors computed with RDKit.¹²⁰ These include atomic number, chirality tag (unspecified, tetrahedral, or other, including octahedral, square planar, allene-type), number of directly-bonded neighbors, number of rings, implicit valence, formal charge, number of attached hydrogens, number of unpaired electrons, hybridization, aromaticity, and presence in rings of specified sizes from 3 to 7. This choice is inspired by EQUIBIND¹²¹ and DIFFDOCK¹¹⁹ and is in line with the improved⁷² features used for 2D-based methods.

The initial node and edge features pass through embeddings to give $\{\mathbf{x}_a^{(1)}\}$ and $\{\mathbf{e}_{ab}\}$

respectively, the former are then updated by $n_{\text{conv}} \in \{2, 3\}$ equivariant convolutional layers. Each layer is a fully-connected weighted tensor product, as defined in `e3nn`.¹¹⁸ Equations S5–S16 describe the equivariant operations performed by the network (see Section S1 for mathematical details). The network with equivariant molecular components as described is referred to as `EQUIREACT`, where its invariant counterpart `INREACT` uses only the $\ell = 0$ (scalar) spherical harmonics to construct the convolution filters. The output of the molecular channels is the local molecular representation $\mathbf{X} \in \mathbb{R}^{N_{\text{at}} \times D}$ corresponding to N_{at} atoms associated with D features. Depending on the `sum_mode` hyperparameter, it is constructed either from the node features (`node` mode) or both node and edge features (`both` mode).

Inspired by the `CHEMPROP` model,^{71,103} we added an option to exclude hydrogen atoms as nodes when constructing the graph. The only information about hydrogens is then contained in the initial edge features of heavy atoms.

2.2 Combining molecules for reactions

Once atom-wise molecular representations \mathbf{X} are learned for reactant and product molecules, they must be combined to form a reaction representation \mathbf{X}_{rxn} .

For certain datasets, atom-mapping information is available, which correlates individual atoms in reactant molecules to individual atoms in product molecules according to the reaction mechanism. In this setting, the representations $\mathbf{X}_{\text{reactant}}$ and $\mathbf{X}_{\text{product}}$ are re-ordered such that the local representation vectors correspond to the same atom in reactants and products. Depending on the `combine_mode` hyperparameter, either a difference is taken between products’ and reactants’ atom representations, or they are summed, averaged, or passed through a multilayer perceptron (MLP). Thus, the local reaction representation \mathbf{X}_{rxn} consists of vectors reflecting how the environment changes in the reaction for each atom. We will refer to this variant of the model, which uses atom-mapping information, as `3DREACTM`. While the current model is unable to treat unbalanced reactions (where there are additional atoms on the left- or right-hand side of the reaction equation), its modification in the spirit

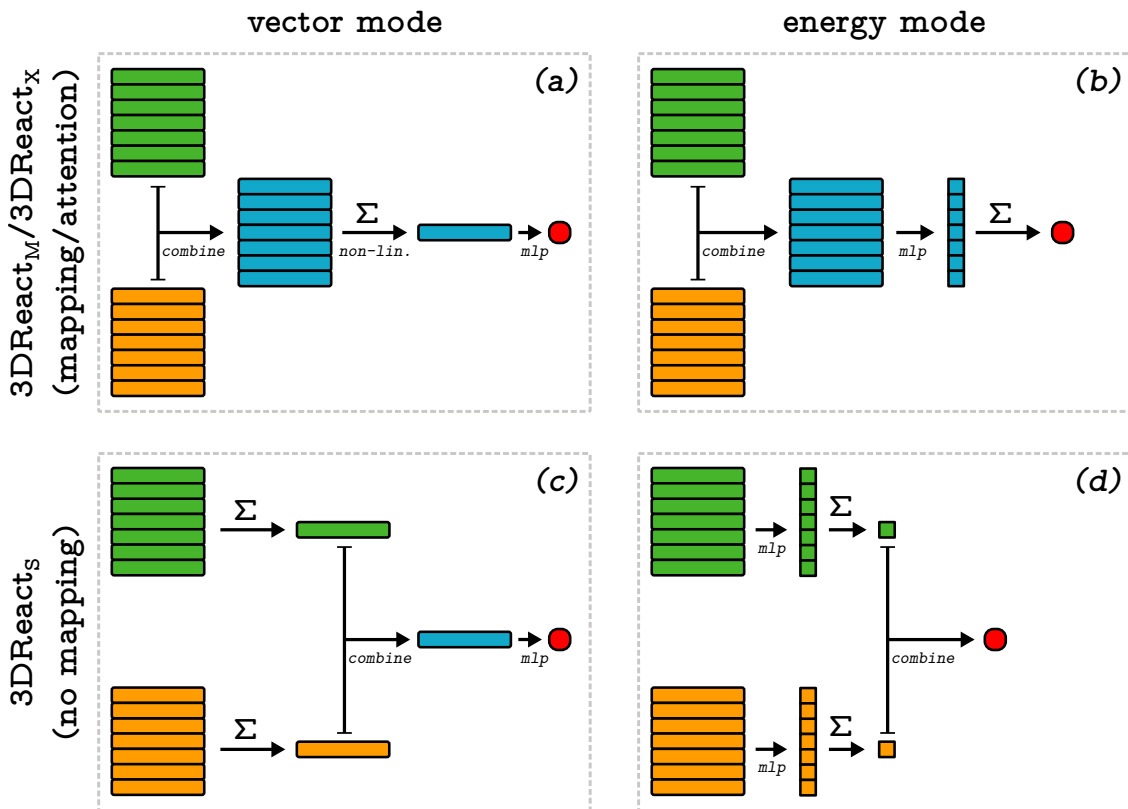


Figure 2: Scheme illustrating how the reactant (green) and product (orange) representations are combined to form a reaction representation (blue) and eventually predict the target property (red dot) using a multilayer perceptron (mlp). Σ refers to the summation over atom-wise environments. Oblong rectangles and squares represent vectors and scalars, respectively.

of CHEMPROP^{71,103} is straightforward.

With the reaction representation at hand, predictions are made in the so-called **vector** or **energy** modes. In **vector** mode, the atomic vectors constituting the reaction representation \mathbf{X}_{rxn} are initially passed through an MLP to introduce nonlinearity and then summed up to form a global reaction representation vector $\bar{\mathbf{X}}_{\text{rxn}}$. The target is then learned using an MLP. This model pipeline is illustrated in Figure 2a. In **energy** mode, on the other hand, the local reaction representations are used to learn atomic contributions to the target (Figure 2b). While performing worse in general, in some cases this mode yields the best predictions (see Section 3.2.1).

Atom-mapping provides *static* information, analogous to a reaction mechanism, to link

atoms in reactants to atoms in products. While highly informative, and thought to be critical to the performance of 2D-graph-based models,^{70–72,81,103} accurate atom-maps are not available for all reaction datasets.^{38,104,105} To circumvent the need for atom-mapping, but mimic its role in exchanging information between reactants and products, other approaches *dynamically* (*i.e.*, in a learnable fashion) exchange information between molecular representations. For example, RXNMAPPER¹⁰⁷ is a neural network that learns atom-mappings within the larger self-supervised task of predicting the randomly masked parts in a reaction sequence, using one head of a multi-head transformer architecture. EQUIBIND,¹²¹ a neural network that predicts the rotation and translation of a ligand to a protein, contains a cross-attention module between ligand and receptor. The latter inspires our surrogate for atom-mapping: 3DREACT_X also uses cross-attention between reactants and products to link their atom indices (Section S4). The re-ordered representations of reactants and products are combined as for the case of atom-mapped reactions (Figures 2a and 2b). We note that other algorithms could also have been used to exchange information between reactants and products, for example in the form of message passing or equivariant attention.^{57,122}

3DREACT also has a simple “no mapping” variant, called 3DREACT_S, which does not rely on atom-mapping, nor a surrogate cross-attention module. In **vector** mode (Figure 2c), the atomic components of molecular representations $\mathbf{X}_{\text{reactant}}$ and $\mathbf{X}_{\text{product}}$ are summed up to obtain global vectors $\bar{\mathbf{X}}_{\text{reactant}}$ and $\bar{\mathbf{X}}_{\text{product}}$, respectively. Then they are combined, according to the `combine_mode` parameter, to form a reaction vector $\bar{\mathbf{X}}_{\text{rxn}}$ which is used to learn the target with an MLP. In **energy** mode (Figure 2d) individual atomic representations are used to learn their contributions to the quasi-molecular energies of reactants and products, which are later combined (according to the `combine_mode` parameter) to predict the target. In most cases, this simpler model out-performs 3DREACT_X (*vide infra*).

3 Results and Discussion

The performance of 3DREACT is reported for three diverse datasets (the GDB7-22-TS,¹¹⁶ Cyclo-23-TS¹¹⁷ and Proparg-21-TS^{69,108}) using both random and extrapolative splits. For details on the datasets, refer to Section 5.1. For details on the extrapolation splits, see Section 5.2.

Models are run in three atom-mapping regimes: (i) with high-quality maps (“True”) derived from the TS structures or heuristic rules;^{71,106,116,117,123} (ii) with atom-maps obtained using the open-source RXNMAPPER¹⁰⁷ (“RXNMapper”); and (iii) without any atom-mapping information at all (“None”). As discussed in recent work,^{38,124} previously developed graph-based models for reaction property prediction^{70–72,96,97} including CHEMPROP^{71,103} reported prediction errors only in the “True” atom-mapping regime. The “RXNMapper” regime is important for cases where the reaction mechanism is not known and atom-mapping using heuristic rules is impossible. The “None” regime is critical for all chemistry that falls outside the realm of organic chemistry captured in the patents¹²⁵ that RXNMAPPER¹⁰⁷ is trained on.

The atom-mapping-based model 3DREACT_M is used in the “True” and “RXNMapper” regimes. In the “None” regime, 3DREACT_X and 3DREACT_S were tested. 3DREACT_S consistently outperformed 3DREACT_X, so we include only 3DREACT_S and refer the reader to Section S4 for their comparison.

3.1 Equivariance *vs.* invariance

Table 1 compares the relative performance of the invariant (INREACT) and the equivariant (EQUIREACT) implementations of 3DREACT with the learning curves of the two models presented in Figure 3. Previous studies^{43,56} demonstrated that the equivariant models showed superior extrapolation capabilities on predictions of energies and forces, as well as steeper and shifted learning curves in force prediction tasks. Instead, we find that INREACT and EQUIREACT are practically indistinguishable for the present chemical reaction tasks.

Table 1: Performance as measured in mean absolute errors (MAEs) of predictions of 3DREACT (INREACT *vs.* EQUIREACT). 3DREACT_M is used for the “True” and “RXN-Mapper” regimes, and 3DREACT_S is used for the “None” regime. MAEs are averaged over 10 folds of 80/10/10 splits (training/validation/test) and reported together with standard deviations across folds.

Dataset (property, units)	Atom-mapping regime	INREACT	EQUIREACT
<i>Random splits</i>			
GDB7-22-TS (ΔE^\ddagger , kcal/mol)	True	4.93 \pm 0.18	4.93 \pm 0.15
	RXNMapper	6.03 \pm 0.26	6.05 \pm 0.25
	None	6.56 \pm 0.26	6.53 \pm 0.28
Cyclo-23-TS (ΔG^\ddagger , kcal/mol)	True	2.39 \pm 0.08	2.30 \pm 0.09
	RXNMapper	2.37 \pm 0.07	2.35 \pm 0.12
	None	2.39 \pm 0.05	2.31 \pm 0.09
Proparg-21-TS (ΔE^\ddagger , kcal/mol)	True	0.33 \pm 0.07	0.31 \pm 0.05
	None	0.34 \pm 0.06	0.31 \pm 0.06
<i>Scaffold splits</i>			
GDB7-22-TS (ΔE^\ddagger , kcal/mol)	True	7.8 \pm 0.7	7.8 \pm 0.8
	RXNMapper	9.2 \pm 0.8	9.1 \pm 0.8
	None	10.1 \pm 0.9	10.0 \pm 0.9
Cyclo-23-TS (ΔG^\ddagger , kcal/mol)	True	2.79 \pm 0.18	2.72 \pm 0.18
	RXNMapper	2.77 \pm 0.22	2.71 \pm 0.23
	None	2.76 \pm 0.22	2.72 \pm 0.19
Proparg-21-TS (ΔE^\ddagger , kcal/mol)	True	0.44 \pm 0.11	0.40 \pm 0.08
	None	0.45 \pm 0.10	0.41 \pm 0.09

We find that the datasets studied herein do not benefit from the inclusion of equivariant features for molecules. Yet, Figure 4 illustrates that a hypothetical reaction involving conversion between homometric structures of He₄,¹²⁶ which is mostly characterized by angle changes, clearly benefits from equivariant molecular features. In the reactant (Figure 4a), all atoms are identical and lead to the same learned representation. In the product (Figure 4b), only atoms B2 and B3 have identical environments, different from A1–4. Atoms B2–3 have the same distances r to the three neighbors, as in A1–4. Thus, INREACT, which uses only

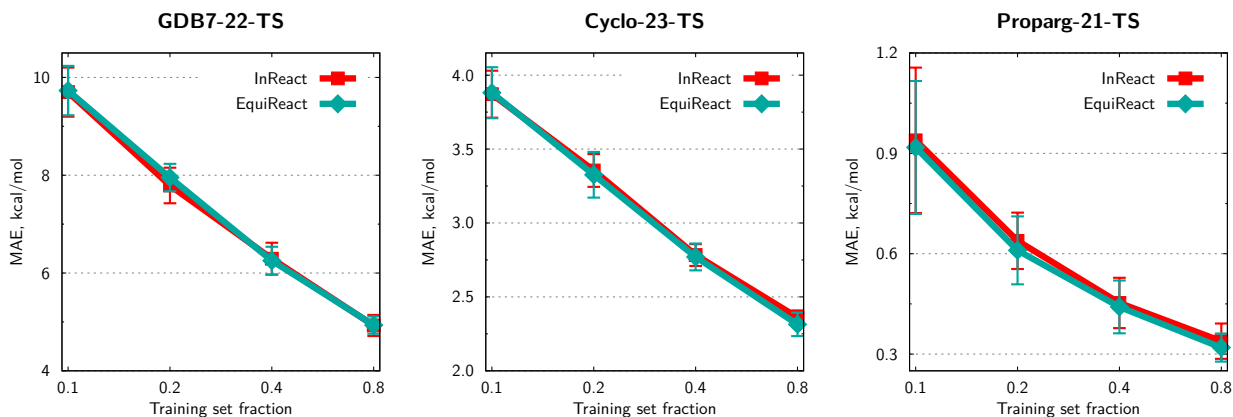


Figure 3: Learning curves for INREACT and EQUIREACT in the “True” atom-mapping regime. Each point shows mean absolute error (MAE), averaged over 10 folds of 80/10/10 splits (for training set fraction < 0.8, the corresponding subset of the “full” training set is used), and error bars indicate standard deviations across folds.

interatomic distances, yields very close representations for these atoms (Figure 4c). Still, in each convolutional layer, atoms B2 and B3 receive information from B1 and B4, and with increase of n_{conv} the difference in the representations of B2–3 and A1–A4 becomes more apparent (Figure 4d). However, with smaller radial cutoff $r_{\text{max}} = 1.9$, atoms B1–B3 and A1–4 become indistinguishable for any number of layers (Figure 4e). On the other hand, EQUIREACT, which uses explicit angular information from the spherical harmonics filters, clearly distinguishes all non-equivalent atoms in both cases already for $n_{\text{conv}} = 2$ (Figure 4f,g).

While this is a toy example, it illustrates that transformations consisting of changes in angles rather than in bond lengths are better described using EQUIREACT. In general, the currently available reaction datasets do not pose sufficient challenge to allow distinguishing INREACT and EQUIREACT. For the datasets studied in this work, INREACT is sufficient and is the model variation used throughout as 3DREACT.

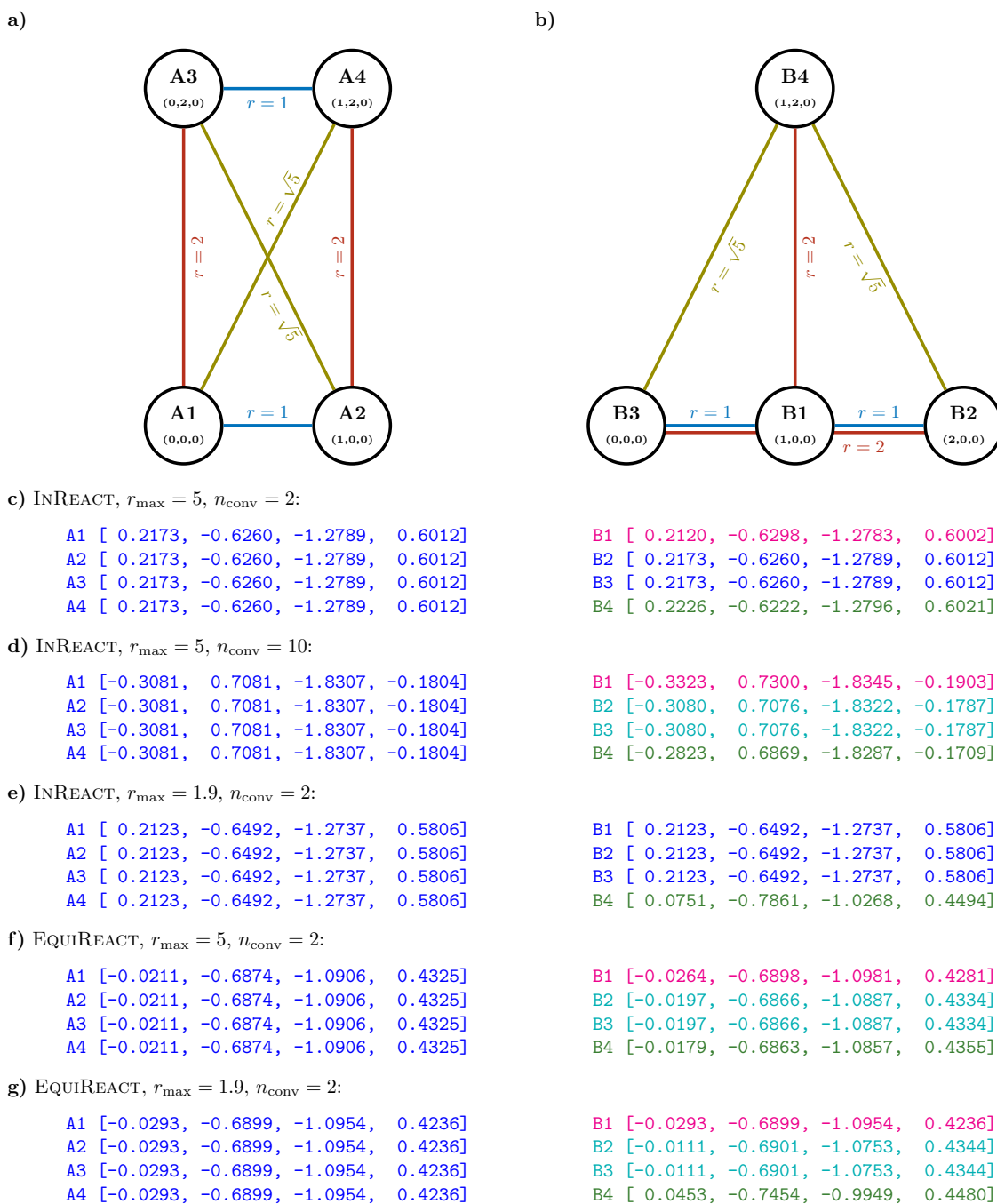


Figure 4: Top: Reactant and product of a toy reaction: two homometric structures (a) and (b) with atom labels, atom coordinates (\AA), and interatomic distances (\AA). “Bonds” of the same length are of the same color. Bottom: output after 5 epochs of the invariant (c,d,e) / equivariant (f,g) molecular channels for each atom with different radial cutoffs r_{\max} and number of convolutional layers n_{conv} . Within each subfigure, atomic representations indistinguishable up to shown digits are marked by the same color.

3.2 Benchmark studies

3DREACT is compared to previously best baseline models:³⁸ CHEMPROP,^{71,103} a graph neural network that uses atom-mapped SMILES to construct a CGR, and the 3D-structure-based SLATM⁸ fingerprint adapted to reactions by taking the difference between product and reactant fingerprints (SLATM_d),³⁶ combined with KRR models (SLATM_d+KRR).

Note that both 3DREACT and CHEMPROP are run without explicit H atoms, for two reasons. First, hydrogen atoms are not always mapped in the “True” and “RXNMapper” regimes, since they are usually implicit in SMILES strings. Second, there is no consistent improvement in including H atoms in the models (Table S6). SLATM_d, built directly from molecular coordinates without using SMILES strings, does however incorporate H atoms by default. For further discussion refer to Section S7.

3.2.1 Random splits

Performance as measured in mean absolute errors (MAEs) is illustrated in Table 2 for random splits of each dataset, demonstrating the models’ interpolative capabilities. For the equivalent results with root mean squared errors (RMSEs), consult Section S3.

The GDB7-22-TS dataset is distinct from the other two in that it includes variations in the reaction class (and mechanism), thereby showing a greater dependence on the existence and quality of atom-mapping information in the models. It has already been observed³⁸ for CHEMPROP that there is stark hierarchy in the predictions from the “True” to “RXNMapper” to “None” regimes.

In the “True” regime, 3DREACT does not improve predictive capabilities over the CHEMPROP model for the GDB7-22-TS set. This points to the importance of the chemical diversity in this dataset, where knowledge of the reaction mechanism (in the form of atom-maps) is sufficient information to predict the reaction barriers without information about the geometries of reactants and products. However, as previously discussed,³⁸ “True” maps are an unrealistic scenario for most datasets. Moving to the “RXNMapper” regime,

Table 2: Performance as measured in mean absolute errors (MAEs) of predictions of 3DREACT *vs.* state-of-the-art baselines CHEMPROP and SLATM_d+KRR. All datasets are compared in three atom-mapping regimes: “True”, “RXNMapper” and “None”, except for the Proparg-21-TS set, where RXNMAPPER cannot map the reaction SMILES. MAEs are averaged over 10 folds of random 80/10/10 splits (training/validation/test) and reported together with standard deviations across folds. The lowest errors for each regime and dataset are highlighted in bold, if statistically relevant.

Dataset (property, units)	Atom-mapping regime	CHEMPROP	SLATM _d +KRR	3DREACT
GDB7-22-TS (ΔE^\ddagger , kcal/mol)	True	4.35 ± 0.15	—	4.93 ± 0.18
	RXNMapper	5.69 ± 0.17	—	6.03 ± 0.26
	None	9.04 ± 0.21	6.89 ± 0.20	6.56 ± 0.26
Cyclo-23-TS (ΔG^\ddagger , kcal/mol)	True	2.69 ± 0.10	—	2.39 ± 0.08
	RXNMapper	2.71 ± 0.07	—	2.37 ± 0.07
	None	2.71 ± 0.12	2.65 ± 0.08	2.39 ± 0.05
Proparg-21-TS (ΔE^\ddagger , kcal/mol)	True	1.53 ± 0.14	—	0.33 ± 0.07
	None	1.56 ± 0.16	0.33 ± 0.04	0.34 ± 0.06

3DREACT and CHEMPROP already agree within standard deviations. This highlights that for practical-quality maps, 3DREACT is amongst the best models for this dataset. In the “None” regime, 3DREACT outperforms CHEMPROP by more than 2 kcal/mol.

SLATM_d+KRR results in similar performance to 3DREACT for the GDB7-22-TS set. The SLATM_d representation also constructs features from 3D coordinates of the reactants and products using invariant functions, and is therefore more fundamentally similar to 3DREACT than CHEMPROP. Nevertheless, since 3DREACT allows for the inclusion of atom-mapping information, predictions are improved in the mapped regimes compared to SLATM_d+KRR, which operates in the “None” regime only.

In summary, for the chemically diverse GDB7-22-TS set, while SLATM_d allows for good performance in the “None” regime, and CHEMPROP in the “True” and “RXNMapper” regimes, since 3DREACT can incorporate both atom-mapping information and 3D structure information, the model achieves robust performance in all three regimes, with the predicted MAEs ranging from 4.93–6.56 kcal/mol.

The Cyclo-23-TS¹¹⁷ dataset contains a single reaction class and has been previously illustrated³⁸ to show less dependence on the quality of atom-mapping than the GDB7-22-TS. For this set, 3DREACT outperforms or matches the other models in all three regimes. This illustrates that a model based purely on geometry information of reactants and products, without any chemical information in the form of atom-mapping or surrogates thereof, can allow for accurate reaction property prediction. It is worth noting that atom-mapping does not improve predictions at all, *i.e.* there is no improvement from “None” to “RXNMapper” to “True”, even for the CHEMPROP model. This points to the different nature of this dataset compared to the GDB7-22-TS.

The best model is obtained with 3DREACT_S in the **energy** mode (Figure 2d). As outlined in Section 2.2, in **energy** mode an energy contribution is learned for reactants’ and products’ atoms separately. In the original publication,¹¹⁷ Stuyver *et al.* illustrate that the activation barriers (ΔG^\ddagger) correlate linearly with the reaction energy (ΔG). Since ΔG is the difference between products’ and reactants’ energies, the **energy** mode is the best choice for a model learning the reaction energy, and in the case of this dataset, for ΔG^\ddagger too, due to its linear correlation with ΔG .

Compared to SLATM_d+KRR, 3DREACT in the “None” regime results in lower prediction errors for this set, illustrating that despite both models using similar information, an end-to-end model can allow for improved predictions.

The Proparg-21-TS^{69,108} is a small dataset for neural network standards (753 points) and therefore constitutes a challenge for the data efficiency of our model. Like the Cyclo-23-TS set, it consists of a single reaction class, *i.e.* enantioselective propargylation of benzaldehyde. Since the enantioselectivity is related to the barrier through an exponential relationship, it is critical to predict the barrier accurately (≤ 1 kcal/mol).⁶⁹ The “RXNMapper” regime is not available since RXNMAPPER cannot atom-map the reaction SMILES of this set.

In the other regimes, 3D-structure-based models lead to the best results, outperforming CHEMPROP by a large margin. Proparg-21-TS is particularly hard for 2D-based models³⁸

since it contains molecules of different stereochemistry but the same SMILES strings. Again trained on a single-reaction class dataset, models do not benefit from being provided the “obvious” chemical information: including true atom-maps does not decrease the error. Competing only in the “None” regime, 3DREACT does not allow for a performance improvement compared to SLATM_d+KRR. Given the small size of the dataset, it is already a demonstration of data efficiency that the deep-learning model matches the prediction errors of the kernel model. Unlike for NEQUIP⁴³ however, the data efficiency here is not due to the equivariant molecular components (Section 3.1).

The three datasets illustrate the benefits of the flexibility of 3DREACT: depending on the datasets’ particular challenges, the model exploits the available information to yield the best-performing model in almost all cases. Since the model settings (such as `vector` or `energy` mode choice) are specified as hyperparameters, the optimized version of 3DREACT can emerge with minimal user intervention.

3.2.2 Extrapolative splits

Figure 5 illustrates model performance for extrapolative splits (based on scaffolds, molecular size of reactants/products, and barrier magnitude, detailed in Section 5.2). These different types of extrapolative splits are necessarily more difficult than random splits, as demonstrated by higher MAEs in Figure 5. The relative performance of the models is largely maintained in the three different extrapolation regimes compared to the interpolation regime presented in Table 2.

Bemis–Murcko scaffold¹²⁷ splitting clusters molecules (reactants for GDB7-22-TS and Proparg-21-TS, products for Cyclo-23-TS) based on ring systems. Test molecules may therefore appear “novel” from the point of view of the reaction graph, but will still feature distances and angles close to what the model has seen during training. Similarly for size-based splits, since there is no correlation between reactant/product size and reaction barriers, using distance information allows for stable predictions on extrapolation. Property-based

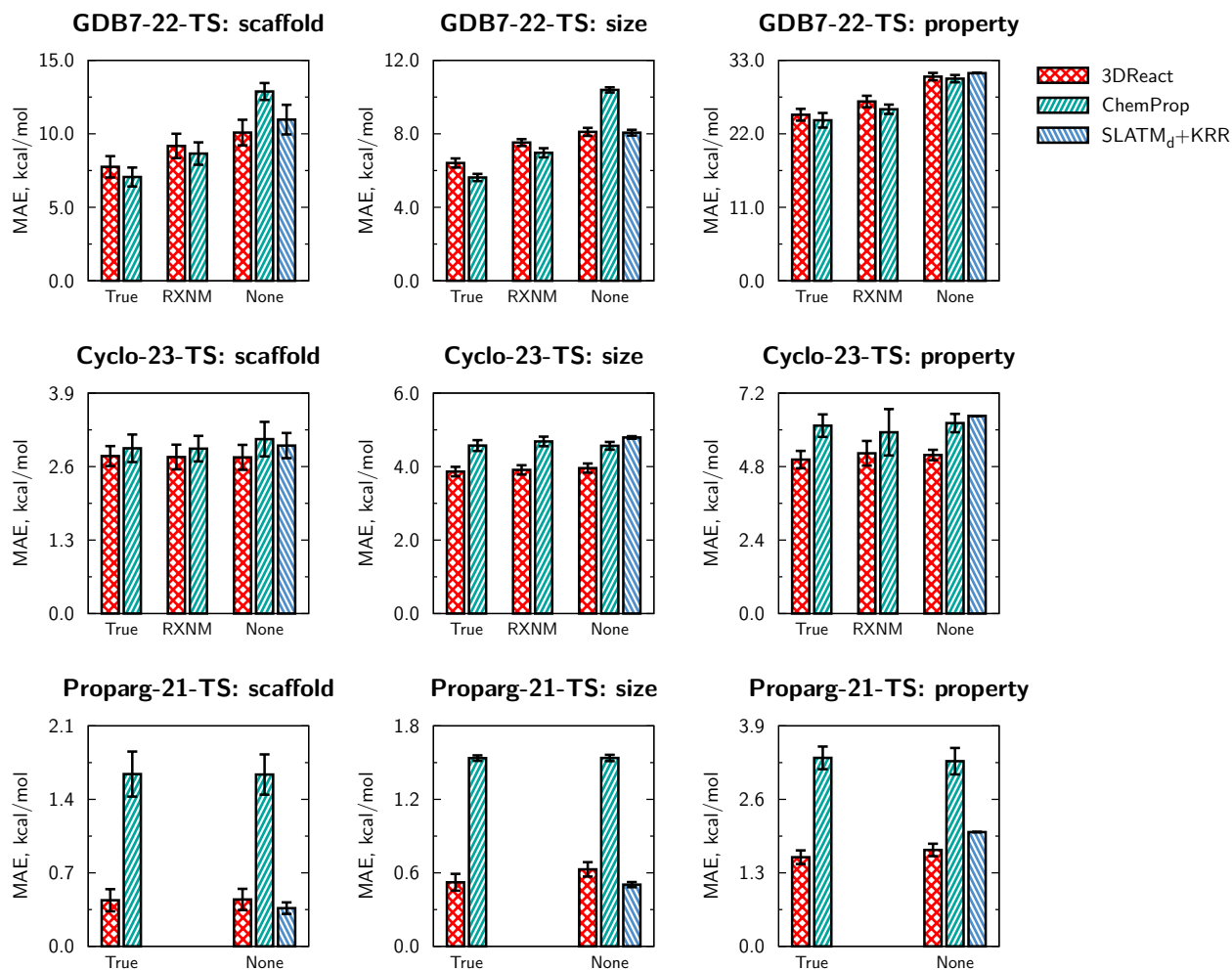


Figure 5: Mean absolute errors (MAEs) of predictions using three different extrapolation splits: scaffold, size-, and property-based. All datasets are compared in three atom-mapping regimes: “True”, “RXNMapper” (RXNM), and “None”, except for the Proparg-21-TS set, where RXNMAPPER cannot map the reaction SMILES. MAEs are averaged over 10 folds of 80/10/10 splits (training/validation/test), and error bars indicate standard deviations across folds, where applicable.

splits are more challenging than the other two. For the Cyclo-23-TS and Proparg-21-TS sets, 3DREACT still offers respectable errors, lower than those of the other models. For the GDB7-22-TS set however, all models result in unreasonable MAEs over 20 kcal/mol. This points to the particular challenges of the GDB7-22-TS set and suggests an avenue for further developments of ML models for extrapolative tasks.⁸¹

Again in contrast to previous works that suggested equivariant models might be better at extrapolation tasks,^{43,56} here we find that 3DREACT offers stable extrapolation performance

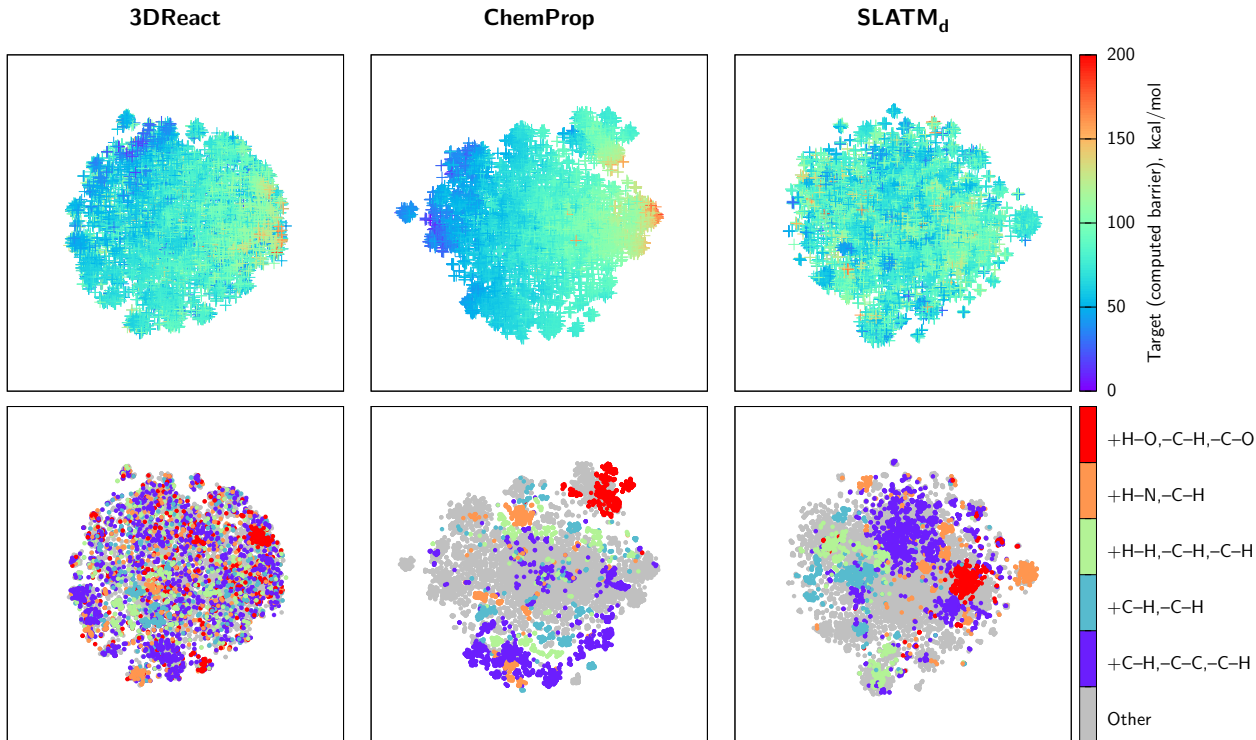


Figure 6: t-SNE maps (perplexity = 64) of the latent representations of 3DREACT and CHEMPROP models in the “True” regime and the SLATM_d representation of the GDB7-22-TS dataset, colored by the target ΔE^\ddagger (upper panels) and reaction types (lower panels).

(particularly for size- and scaffold-based splits), but not necessarily improved extrapolation behavior compared to 2D-graph based models. This points to the different challenges in reaction property prediction. Nevertheless, Figure 5 illustrates that 3DREACT is a consistently robust model for the three datasets when moving from interpolation to extrapolation regimes.

3.3 Model behavior

Since the GDB7-22-TS set has the largest chemical diversity amongst the datasets explored, studying 3DREACT and baseline models SLATM_d and CHEMPROP on this dataset best captures the different chemical interpretation provided by these models.

Figure 6 compares the (latent) representations of 3DREACT “True”, CHEMPROP “True” and SLATM_d using t-SNE¹²⁸ maps. In the upper panel, we find that the quality of the

correlation between the representations and the target property are aligned with the relative performance of the models (Table 2). CHEMPROP and 3DREACT show a smooth transition of the target property, whereas the map of SLATM_d does not have a clear structure. The lower panel shows the correlation of the representations with the five most common reaction types defined by bond breaking and formation (see Section 5.4). CHEMPROP, as a chemically-inspired model, illustrates clear clusters in the reaction type. While SLATM_d is a geometry-based model, the binning structure used to create the representation^{8,36} results in a clear correlation with the reaction types, since *e.g.* the pairwise bins naturally cluster features such as C–H bond formation or breaking. 3DREACT shows the least distinct “chemical” clustering, due to the interplay of geometry and mapping information exploited in the representation.

Figure 7 shows the error distribution of predictions belonging to the same reaction classes for 3DREACT “True”. 3DREACT performs universally well across the different reaction types, with consistently low errors and relatively small error spread. The reactions for which the model has higher mean errors and spread (+H–H, –C–H, –C–H (green)) correspond to those involving C–H and H–H features. Since the model is trained without explicit H nodes in the graph, features associated with X–H bonds are included implicitly in the model. Capturing H–H bond changes will be the most challenging as these will be the least explicitly described, occurring only as initial features for neighboring nodes. Since C is the most frequently occurring element in various different configurations, capturing all the C–H features is more challenging than the O–H features for example, which will be more similar to one another. The equivalent plot for the model trained with explicit H nodes is shown in Figure S4, illustrating that the error spread reduces for the reaction types involving C–H and H–H features. Note that 3DREACT without explicit Hs still leads to performance comparable to the variant with explicit Hs (Section S7).

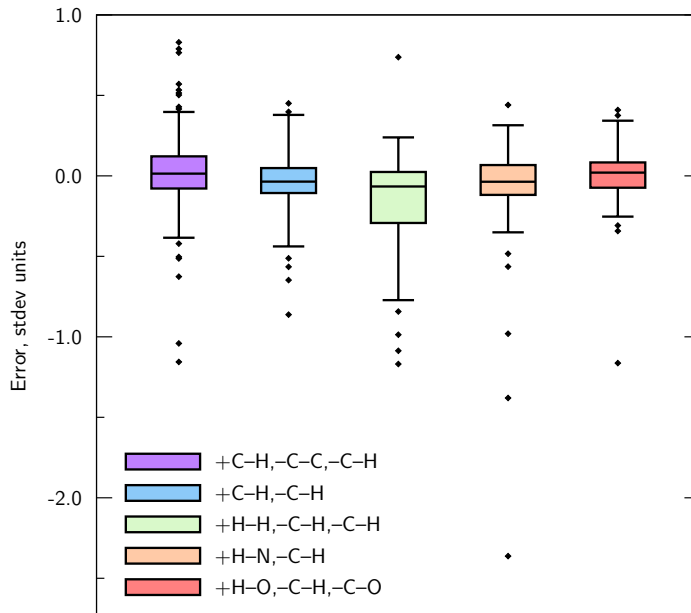


Figure 7: Box plots illustrating how 3DREACT “True” performs for the most common reaction types in the GDB7-22-TS set. 3DREACT is constructed without explicit H nodes in the graphs. The boxes range from the first to the third quartile of the datapoints. The whiskers limit 90% of the datapoints and the individual points illustrate outliers. The points correspond to the test set of the first random split. The errors are given in the target standard deviation (stdev) units (21.8 kcal/mol).

3.4 Geometry quality

In order to illustrate that 3DREACT does not require high-quality molecular structures to be used in an out-of-sample scenario, we train and test a model using lower-quality GFN2-xTB¹²⁹ (xTB) geometries to predict higher-level barriers (CCSD(T)-F12a/cc-pVDZ-F12// ω B97X-D3/def2-TZVP for GDB7-22-TS, B3LYP-D3(BJ)/def2-TZVP//B3LYP-D3(BJ)/def2-SVP for Cyclo-23-TS and B97D/TZV(2p,2d) for Proparg-21-TS). The results are illustrated in Figure 8 for the three datasets with DFT and xTB geometries, and compared to the SLATM_d+KRR model in the same settings. 3DREACT benefits from a lower sensitivity to the geometry quality compared to the pre-designed representation SLATM_d combined with KRR, across the three datasets.

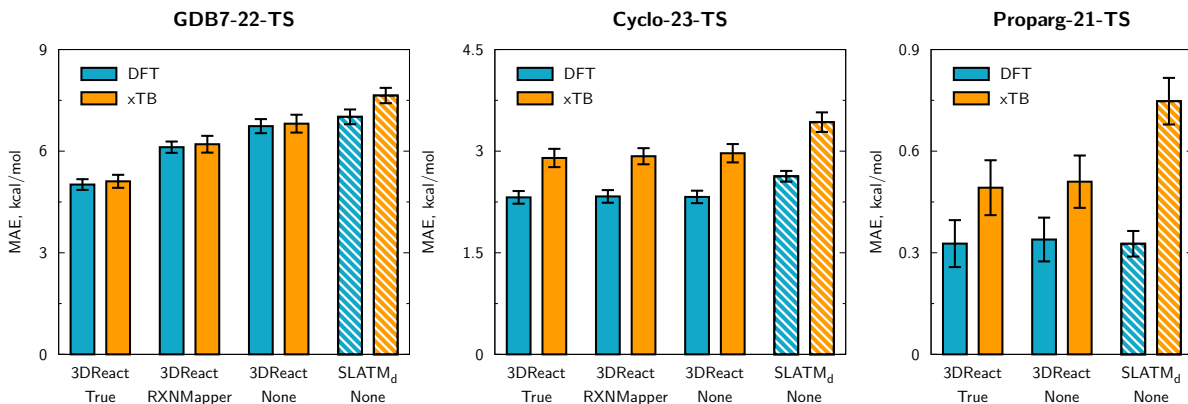


Figure 8: Mean absolute errors (MAEs) for predictions using either the provided geometries (ω B97X-D3/def2-TZVP for GDB7-22-TS, B3LYP-D3(BJ)/def2-SVP for Cyclo-23-TS, B97D/TZV(2p,2d) for Proparg-21-TS) (DFT) or lower-quality GFN2-xTB (xTB) geometries. MAEs are averaged over 10 folds of random 80/10/10 splits (training/validation/test), error bars showing standard deviations across folds. Note that for GDB7-22-TS and Cyclo-23-TS datasets the DFT results are different from those presented in Section 3.2.1 because here they are obtained on the same subset as the xTB results (see Section 5.4).

For the GDB7-22-TS set, there is a negligible difference in model performance moving from DFT to xTB geometries. The xTB geometries are a good proxy for the DFT ones here, since this set consists of small, charge-neutral organic molecules, which are largely well-described by semi-empirical methods. For the Cyclo-23-TS set, while the molecules are still organic, they are larger than those in the GDB7-22-TS set, and there is a greater divergence between the GFN2-xTB and DFT geometries, resulting in a larger deterioration with these structures. Figure S5 demonstrates that when using the model trained on xTB geometries, barrier predictions for molecules with poorer geometries (*i.e.*, higher RMSD of xTB *vs.* DFT geometries) are not necessarily worse than those on molecules with better geometries. Instead, there is a consistent decline in model performance when training with xTB geometries and predicting DFT barriers.

The Proparg-21-TS set is the most complex of the three for GFN2-xTB, since these systems with charged organosilicon compounds differ considerably from those used to parameterize semi-empirical methods or force fields. As described in Section 5.4, unlike for the other datasets where we generate an initial structure from SMILES using force fields,

for this set it is impossible and we instead generate xTB geometries from the DFT ones. While this is not a feasible geometry generation pipeline for out-of-sample predictions, it still demonstrates how different methods perform with high and low-quality geometries. Here, we see that 3DREACT is less sensitive than SLATM_d+KRR and the variation trained with lower quality geometries still offers competitive errors (0.48 ± 0.05 kcal/mol for the “None” model).

4 Conclusions

The accurate and reliable prediction of reaction barriers across diverse sets of chemical reactions remains an open challenge in computational chemistry. We contribute to this domain by introducing 3DREACT, a geometric deep learning model constructed from the 3D coordinates of reactants and products. We show that the invariant model (*vs.* the equivariant version) is already sufficient for currently available reaction datasets. Existing models CHEMPROP and SLATM_d+KRR exhibit impressive performance for atom-mapped, chemically diverse datasets and stereochemistry-sensitive datasets, respectively. 3DREACT offers a hybrid model that can optionally incorporate mapping information alongside geometries, enabling robust performance across different dataset types and atom-mapping regimes. 3DREACT also allows for a reduced sensitivity to the training geometry quality (*i.e.*, xTB *vs.* DFT level) compared to SLATM_d+KRR. Predictions are stable both when moving to molecular size- or scaffold-based splits. Altogether, 3DREACT presents a flexible framework for accurate prediction of activation barriers across chemical reaction datasets. Despite the proposed developments, challenges remain for ML predictions of energy barriers, particularly in integrating them within experimental settings. This work is a step toward their reliable application.

5 Methods

5.1 Datasets

We test 3DREACT on three datasets of reaction barriers previously used to benchmark reaction representations.³⁸ The term “reaction barrier”, used interchangeably with “activation energy” and “activation barrier” is the energy difference between the energy of the optimized TS and the optimized reactants. Note that depending on the dataset, some provide purely electronic energies (labelled ΔE^\ddagger) and others — Gibbs free energies (labelled ΔG^\ddagger). In all datasets, optimized three-dimensional structures of reactants and products are provided, which are used to train models and make predictions. The activation barrier is not a direct function of these structures, but using the TS structure to make predictions removes the utility of the ML models *vs.* direct computation of the TS. Thus we use an implicit interpolation of reactants’ and products’ structures as a proxy for the TS as in previous works.^{36,38,69}

The GDB7-22-TS¹¹⁶ dataset consists of close to 12 000 diverse organic reactions automatically constructed from the GDB7 dataset^{130–132} using the growing string method¹³³ along with corresponding energy barriers (ΔE^\ddagger) computed at the CCSD(T)-F12a/cc-pVDZ-F12// ω B97X-D3/def2-TZVP level. The dataset provides atom-mapped SMILES, with “True” maps derived from the transition state. For 43 reactions out of 11 926, one of the products’ SMILES represents a molecule different from the xyz structure. These reactions were therefore excluded from the dataset, leading to a modified GDB7-22-TS set used here.

While there are no pre-defined classes for all the reactions in the GDB7-20-TS¹²³ or GDB7-22-TS¹¹⁶ sets, Grambow *et al.*⁷⁰ split the dataset into reactions undergoing certain bond changes: for example, the most common type was breaking of a C–H bond (–C–H) and a C–C bond (–C–C) in the reactants and formation of a C–H bond (+C–H) in the products, giving the reaction type signature +C–H,–C–C,–C–H. Here, we extract similar reaction types by comparing the connectivity matrices from atom-mapped reaction SMILES of reactants and products (ignoring bond orders). The most abundant reaction types in the

dataset are +C-H,-C-C,-C-H (1667 reactions), +H-N,-C-H (633), +C-H,-C-H (619), +H-O,-C-H,-C-O (599) and +H-H,-C-H,-C-H (517).

The original Cyclo-23-TS¹¹⁷ dataset encompasses 5 269 profiles for [3 + 2] cycloaddition reactions with activation free energies (ΔG^\ddagger) computed at the B3LYP-D3(BJ)/def2-TZVP//B3LYP-D3(BJ)/def2-SVP level in water using the SMD continuum solvation model. The dataset provides atom-mapped SMILES with “True” maps for heavy atoms derived from either the transition state structure or heuristic rules. For the regime with explicit hydrogen atoms, we atom-mapped the xyz files by matching the reactants, given in two separate files, to the provided transition state structure, which closely resembles the two reactants and has the same atom order as in the product. This was done with a labelled graph matching algorithm as implemented in **NetworkX**.^{134,135} The algorithm is unaware of chirality, double-bond stereochemistry or conformations, and thus may lead to not exactly correct atom-mappings. We also found that in four reactions, the product SMILES and xyz files depict different species, thus the set was reduced to 5 265 reactions.

The Proparg-21-TS dataset^{69,108} contains 753 structures of intermediates before and after the enantioselective transition state of benzaldehyde propargylation, with activation energies (ΔE^\ddagger) computed at the B97D/TZV(2p,2d) level. SMILES strings (“fragment-based” SMILES) and “True” atom-maps are not provided with the original dataset, these are taken from Ref. 38.

RXNMAPPER¹⁰⁷-mapped versions of GDB7-22-TS and Cyclo-23-TS were obtained with the python package `rxnmapper` (version 0.3.0), using the default settings. The Proparg-21-TS set cannot be mapped, because the underlying libraries cannot process its SMILES string.³⁸ Since RXNMAPPER sorts molecules in case of multiple reactants and/or products, which would complicate SMILES-xyz matching (see Section 5.3 below), we used a locally modified version that does not change the molecule order (the patch file is provided in the project repository at <https://github.com/lcmd-epfl/EquiReact/tree/9d78892fe/data-curation/rxnmapper>).

5.2 Data splits

For each dataset and splitting type, identical data splits were used for all the models compared. In each case, ten different splits are constructed with different random seeds.

Three different types of extrapolation split were used: scaffold-, molecular size- and property-based. Scaffold splitting^{136,137} clusters molecules based on their 2D backbones (such as Bemis–Murcko scaffolds¹²⁷) and ensures that the clusters (scaffolds) belonging to the training, validation, and test sets do not overlap. Size-based splitting organizes the splits such that the reactions of the smallest molecules are in the training set and the reactions of the largest molecules are in validation and test. With property-based splits, one trains on reactions with higher barriers and predicts on reactions with lower barriers. This choice of splits reflects the relevant out-of-sample cases: larger molecules are more expensive to compute, and reactions with smaller barriers are desirable. Size- and property-based splits can also be organized in reverse order, where larger molecules are in the train set and smaller in test, or reactions with lower barrier in train and higher barrier in test.

For molecular size- and scaffold-based splits, the initial data shuffling affects the composition of the datasets. The non-zero standard deviations for property-based splits with neural networks arise from different organization of the datapoints into batches.

5.3 Matching SMILES strings to xyz geometries

3DREACT makes use of both the graph structure of a molecule (as provided in the SMILES string) and the three-dimensional structure (in the xyz). The atoms in the graph are associated with the atomic coordinates provided in the xyz file. Thanks to the way the GDB7-22-TS dataset¹¹⁶ was generated, the atomic coordinates can be easily matched to SMILES which in turn allows to atom-map reactants to products. However, we also tested RXNMAPPER-mapped SMILES which do not respect the same constraints. Therefore, for consistency, we use a SMILES–xyz matching procedure detailed below.

We construct molecular graphs from xyz using covalent radii and matched them to

RDKit¹²⁰ molecular graphs obtained from SMILES with a labelled graph matching algorithm as implemented in NetworkX.^{134,135} This procedure is however unaware of chirality and double-bond stereochemistry, thus some of the matches might be incorrect. Still, it provides a flexible method that can be applied to any dataset consisting of SMILES strings and xyz files.

The same procedure was applied to the Cyclo-23-TS dataset in the few cases when the canonical SMILES have a different atom ordering than xyz.

5.4 xTB geometry generation

For the GDB7-22-TS and Cyclo-23-TS datasets, the starting structures were generated from SMILES using the distance-geometry embedding implemented in RDKit¹²⁰ with the srETKDGv3 settings.¹³⁸ Ten conformations were produced per molecule, which were then energy-ranked with the MMFF94 implementation¹³⁹ in RDKit, defaulting to UFF in case of missing parameters. The lowest energy conformer was retained. For the Proparg-21-TS set, the original B97D/TZV(2p,2d) geometries were used as a starting point, because the stereochemical and conformational diversity of this set cannot be completely encoded with SMILES. Therefore MMFF94 will fail to generate an initial geometry from SMILES.

For all the sets, the starting structures were optimized at the GFN2-xTB semi-empirical level of theory¹²⁹ at the “loose” convergence level for a maximum of 1000 iterations using xTB¹⁴⁰ version 6.2 RC2. For 969 reactions of the GDB7-22-TS set and 491 reactions of the Cyclo-23-TS set, at least one of the participating molecules either could not converge to any reasonable configuration or converged to a structure not matching the SMILES. These reactions were excluded from the geometry quality tests (Section 3.4).

5.5 Model training

3DREACT was trained using the Adam optimizer¹⁴¹ with initial learning rate and weight decay parameters as hyperparameters. The learning rate was reduced by 40% after 60 epochs

of no improvement in the validation MAE, as in Ref. 121. Models were trained for max. 512 epochs, using early stopping after 150 epochs of no improvement. The model with the best validation score was then used to make predictions on the test set.

The optimal model hyperparameters were searched within the following values: learning rate $\in [5 \cdot 10^{-5}, 10^{-4}, 5 \cdot 10^{-4}, 10^{-3}]$; weight decay parameter $\in [10^{-5}, 10^{-4}, 10^{-3}, 0]$; node and edge features embedding size $n_s \in [16, 32, 48, 64]$; $\ell=1$ hidden space size $n_v \in [16, 32, 48, 64]$; number of edge features $n_g \in [16, 32, 48, 64]$; number of convolutional layers $n_{\text{conv}} \in [2, 3]$; radial cutoff $r_{\text{max}} \in [2.5, 5.0, 10.0]$; maximum number of atom neighbors $n_{\text{neigh}} \in [10, 25, 50]$; dropout probability $p_d \in [0.0, 0.05, 0.1]$; `sum_mode` $\in [\text{node}, \text{both}]$; `combine_mode` $\in [\text{mlp}, \text{diff}, \text{mean}, \text{sum}]$; `graph_mode` $\in [\text{energy}, \text{vector}]$.

The hyperparameter search was done for the equivariant model `EQUIREACTS` (without attention or mapping) using Bayesian search as implemented in Weights & Biases.¹⁴² Hydrogen atoms were excluded from the graphs. Sweeps were run for 128 epochs for the GDB7-22-TS and Proparg-21-TS sets, and for 256 epochs for the Cyclo-23-TS set on the first random split. The parameters resulting in the best validation error, summarized in Table S1, were used for all the other model settings.

5.6 Baseline models

The CHEMPROP model¹⁰³ is based on a CGR built from atom-mapped SMILES strings of reactants and products, which is then passed through the directed message-passing neural network `chemprop`^{71,103,137} (version 1.5.0). The hyperparameters are taken from Ref. 38.

Molecular SLATM vectors were generated using the `qml` python package¹⁴³ before being combined to form the reaction version `SLATMd`. `SLATMd` is used with kernel ridge regression (KRR) models. The kernel functions and widths, and regularization parameters, were optimized on the first of the ten random splits, in line with how the hyperparameters were optimized for 3DREACT. Unlike 3DREACT, the hyperparameters for DFT and xTB geometries were optimized separately.

Data and Software Availability statement

The code is available as a GitHub repository at <https://github.com/lcmd-epfl/EquiReact>. The versions of the datasets used, as well as any processing applied to them, can be found in the same repository. The unprocessed results are available in the same same repository as well as at <https://wandb.ai/equireact>.

Supporting Information Available

Supplementary Information is provided in the freely available file `equireact_si.pdf`, detailing the architecture of the molecular channels (Section S1), the 3DREACT hyperparameters (Section S2), the RMSE analogue of Table 2 (Section S3), the discussion of the model with a cross-attention surrogate for atom-mapping (Section S4), extrapolation studies (Section S5), some illustrative correlation plots for the GDB7-22-TS set (Section S6), the model performance with and without explicit hydrogen atoms (Section S7), and the geometry sensitivity analysis for the Cyclo-23-TS set (Section S8).

Author Information

Author contributions

P.v.G., K.R.B., and C.B. conceptualized the project. 3DREACT and support codes were written and run by K.R.B. and P.v.G., with design suggestions from C.B., V.R.S., and R.L. Results were analyzed by P.v.G., K.R.B., V.R.S., R.L., and C.B. xTB computations were run by R.L. The original draft was written by P.v.G. and K.R.B. with reviews and edits from all authors. C.C. and A.K. provided supervision and acquired funding.

Conflict of interest

The authors have no conflicts to disclose.

Acknowledgement

The authors thank Liam Marsh and Yannick Calvino Alonso for helpful discussion and comments on the text. P.v.G., C.B., V.R.S., R.L., A.K., and C.C. acknowledge the National Centre of Competence in Research (NCCR) “Sustainable chemical process through catalysis (Catalysis)”, grant number 180544, of the Swiss National Science Foundation (SNSF) for financial support. K.R.B. and C.C. were supported by the European Research Council (grant number 817977) and by the National Centre of Competence in Research (NCCR) “Materials’ Revolution: Computational Design and Discovery of Novel Materials (MARVEL)”, grant number 205602, of the Swiss National Science Foundation.

References

- (1) Behler, J.; Parrinello, M. Generalized neural-network representation of high-dimensional potential-energy surfaces. *Phys. Rev. Lett.* **2007**, *98*, 146401.
- (2) Rupp, M.; Tkatchenko, A.; Müller, K.-R.; von Lilienfeld, O. A. Fast and accurate modeling of molecular atomization energies with machine learning. *Phys. Rev. Lett.* **2012**, *108*, 058301.
- (3) Bartók, A. P.; Kondor, R.; Csányi, G. On representing chemical environments. *Phys. Rev. B* **2013**, *87*, 184115.
- (4) Hansen, K.; Biegler, F.; Ramakrishnan, R.; Pronobis, W.; von Lilienfeld, O. A.; Müller, K.-R.; Tkatchenko, A. Machine learning predictions of molecular properties:

- Accurate many-body potentials and nonlocality in chemical space. *J. Phys. Chem. Lett.* **2015**, *6*, 2326–2331.
- (5) Huo, H.; Rupp, M. Unified representation for machine learning of molecules and crystals. *arXiv preprint* **2017**, arXiv:1704.06439.
- (6) Faber, F. A.; Christensen, A. S.; Huang, B.; von Lilienfeld, O. A. Alchemical and structural distribution based representation for universal quantum machine learning. *J. Chem. Phys.* **2018**, *148*, 241717.
- (7) Christensen, A. S.; Bratholm, L. A.; Faber, F. A.; von Lilienfeld, O. A. FCHL revisited: Faster and more accurate quantum machine learning. *J. Chem. Phys.* **2020**, *152*, 044107.
- (8) Huang, B.; von Lilienfeld, O. A. Quantum machine learning using atom-in-molecule-based fragments selected on the fly. *Nat. Chem.* **2020**, *12*, 945–951.
- (9) Drautz, R. Atomic cluster expansion for accurate and transferable interatomic potentials. *Phys. Rev. B* **2019**, *99*, 014104.
- (10) Dusson, G.; Bachmayr, M.; Csányi, G.; Drautz, R.; Etter, S.; van der Oord, C.; Ortner, C. Atomic cluster expansion: Completeness, efficiency and stability. *J. Comput. Phys.* **2022**, *454*, 110946.
- (11) Grisafi, A.; Ceriotti, M. Incorporating long-range physics in atomic-scale machine learning. *J. Chem. Phys.* **2019**, *151*, 204105.
- (12) Grisafi, A.; Nigam, J.; Ceriotti, M. Multi-scale approach for the prediction of atomic scale properties. *Chem. Sci.* **2021**, *12*, 2078–2090.
- (13) Nigam, J.; Pozdnyakov, S.; Ceriotti, M. Recursive evaluation and iterative contraction of N -body equivariant features. *J. Chem. Phys.* **2020**, *153*, 121101.

- (14) Fabrizio, A.; Briling, K. R.; Corminboeuf, C. SPA^{HM}: the Spectrum of Approximated Hamiltonian Matrices representations. *Digital Discovery* **2022**, *1*, 286–294.
- (15) Briling, K. R.; Calvino Alonso, Y.; Fabrizio, A.; Corminboeuf, C. SPA^{HM(a,b)}: Encoding the density information from guess Hamiltonian in quantum machine learning representations. *J. Chem. Theory Comput.* **2024**, *20*, 1108–1117.
- (16) Karandashev, K.; von Lilienfeld, O. A. An orbital-based representation for accurate quantum machine learning. *J. Chem. Phys.* **2022**, *156*, 114101.
- (17) Llenga, S.; Gryn’ova, G. Matrix of orthogonalized atomic orbital coefficients representation for radicals and ions. *J. Chem. Phys.* **2023**, *158*, 214116.
- (18) Li, Z.; Kermode, J. R.; De Vita, A. Molecular dynamics with on-the-fly machine learning of quantum-mechanical forces. *Phys. Rev. Lett.* **2015**, *114*, 096405.
- (19) Chmiela, S.; Tkatchenko, A.; Sauceda, H. E.; Poltavsky, I.; Schütt, K. T.; Müller, K.-R. Machine learning of accurate energy-conserving molecular force fields. *Sci. Adv.* **2017**, *3*, e1603015.
- (20) Chmiela, S.; Sauceda, H. E.; Müller, K.-R.; Tkatchenko, A. Towards exact molecular dynamics simulations with machine-learned force fields. *Nat. Commun.* **2018**, *9*, 3887.
- (21) Behler, J. First principles neural network potentials for reactive simulations of large molecular and condensed systems. *Angew. Chem. Int. Ed.* **2017**, *56*, 12828–12840.
- (22) Smith, J. S.; Nebgen, B.; Lubbers, N.; Isayev, O.; Roitberg, A. E. Less is more: Sampling chemical space with active learning. *J. Chem. Phys.* **2018**, *148*, 241733.
- (23) Bereau, T.; Andrienko, D.; von Lilienfeld, O. A. Transferable atomic multipole machine learning models for small organic molecules. *J. Chem. Theory Comput.* **2015**, *11*, 3225–3233.

- (24) Grisafi, A.; Wilkins, D. M.; Csányi, G.; Ceriotti, M. Symmetry-adapted machine learning for tensorial properties of atomistic systems. *Phys. Rev. Lett.* **2018**, *120*, 036002.
- (25) Wilkins, D. M.; Grisafi, A.; Yang, Y.; Lao, K. U.; DiStasio Jr, R. A.; Ceriotti, M. Accurate molecular polarizabilities with coupled cluster theory and machine learning. *Proc. Natl. Acad. Sci. U.S.A.* **2019**, *116*, 3401–3406.
- (26) Montavon, G.; Rupp, M.; Gobre, V.; Vazquez-Mayagoitia, A.; Hansen, K.; Tkatchenko, A.; Müller, K.-R.; von Lilienfeld, O. A. Machine learning of molecular electronic properties in chemical compound space. *New J. Phys.* **2013**, *15*, 095003.
- (27) Mazouin, B.; Schöpfer, A. A.; von Lilienfeld, O. A. Selected machine learning of HOMO–LUMO gaps with improved data-efficiency. *Mater. Adv.* **2022**, *3*, 8306–8316.
- (28) Brockherde, F.; Vogt, L.; Li, L.; Tuckerman, M. E.; Burke, K.; Müller, K.-R. Bypassing the Kohn-Sham equations with machine learning. *Nat. Commun.* **2017**, *8*, 872.
- (29) Grisafi, A.; Fabrizio, A.; Meyer, B.; Wilkins, D. M.; Corminboeuf, C.; Ceriotti, M. Transferable machine-learning model of the electron density. *ACS Cent. Sci.* **2019**, *5*, 57–64.
- (30) Fabrizio, A.; Grisafi, A.; Meyer, B.; Ceriotti, M.; Corminboeuf, C. Electron density learning of non-covalent systems. *Chem. Sci.* **2019**, *10*, 9424–9432.
- (31) Musil, F.; Grisafi, A.; Bartók, A. P.; Ortner, C.; Csányi, G.; Ceriotti, M. Physics-inspired structural representations for molecules and materials. *Chem. Rev.* **2021**, *121*, 9759–9815.
- (32) Langer, M. F.; Goessmann, A.; Rupp, M. Representations of molecules and materials for interpolation of quantum-mechanical simulations via machine learning. *npj Comput. Mater.* **2022**, *8*, 41.

- (33) Huang, B.; von Lilienfeld, O. A. Ab initio machine learning in chemical compound space. *Chem. Rev.* **2021**, *121*, 10001–10036.
- (34) Kulik, H. J.; Hammerschmidt, T.; Schmidt, J.; Botti, S.; Marques, M. A. L.; Boley, M.; Scheffler, M.; Todorović, M.; Rinke, P.; Oses, C. et al. Roadmap on Machine learning in electronic structure. *Electron. Struct.* **2022**, *4*, 023004.
- (35) Glielmo, A.; Sollich, P.; De Vita, A. Accurate interatomic force fields via machine learning with covariant kernels. *Phys. Rev. B* **2017**, *95*, 214302.
- (36) van Gerwen, P.; Fabrizio, A.; Wodrich, M. D.; Corminboeuf, C. Physics-based representations for machine learning properties of chemical reactions. *Mach. Learn.: Sci. Technol.* **2022**, *3*, 045005.
- (37) Faber, F. A.; Hutchison, L.; Huang, B.; Gilmer, J.; Schoenholz, S. S.; Dahl, G. E.; Vinyals, O.; Kearnes, S.; Riley, P. F.; von Lilienfeld, O. A. Prediction errors of molecular machine learning models lower than hybrid DFT error. *J. Chem. Theory Comput.* **2017**, *13*, 5255–5264.
- (38) van Gerwen, P.; Briling, K. R.; Calvino Alonso, Y.; Franke, M.; Corminboeuf, C. Benchmarking machine-readable vectors of chemical reactions on computed activation barriers. *Digital Discovery* **2024**, *3*, 932–943.
- (39) Schütt, K.; Kindermans, P.-J.; Sauceda Felix, H. E.; Chmiela, S.; Tkatchenko, A.; Müller, K.-R. SchNet: A continuous-filter convolutional neural network for modeling quantum interactions. *Adv. Neural Inf. Process. Syst.* **2017**, *30*, 991–1001.
- (40) Unke, O. T.; Meuwly, M. PhysNet: A neural network for predicting energies, forces, dipole moments, and partial charges. *J. Chem. Theory Comput.* **2019**, *15*, 3678–3693.
- (41) Gasteiger, J.; Groß, J.; Günnemann, S. Directional message passing for molecular graphs. *arXiv preprint* **2020**, arXiv:2003.03123.

- (42) Gilmer, J.; Schoenholz, S. S.; Riley, P. F.; Vinyals, O.; Dahl, G. E. Neural message passing for quantum chemistry. Proceedings of the 34th International Conference on Machine Learning. 2017; pp 1263–1272.
- (43) Batzner, S.; Musaelian, A.; Sun, L.; Geiger, M.; Mailoa, J. P.; Kornbluth, M.; Molinari, N.; Smidt, T. E.; Kozinsky, B. E(3)-equivariant graph neural networks for data-efficient and accurate interatomic potentials. *Nat. Commun.* **2022**, *13*, 2453.
- (44) Gastegger, J.; Becker, F.; Günnemann, S. GemNet: Universal directional graph neural networks for molecules. *Adv. Neural Inf. Process. Syst.* **2021**, *34*, 6790–6802.
- (45) Haghightalari, M.; Li, J.; Guan, X.; Zhang, O.; Das, A.; Stein, C. J.; Heidar-Zadeh, F.; Liu, M.; Head-Gordon, M.; Bertels, L. et al. Newtonnet: A newtonian message passing network for deep learning of interatomic potentials and forces. *Digital Discovery* **2022**, *1*, 333–343.
- (46) Qiao, Z.; Welborn, M.; Anandkumar, A.; Manby, F. R.; Miller, T. F. OrbNet: Deep learning for quantum chemistry using symmetry-adapted atomic-orbital features. *J. Chem. Phys.* **2020**, *153*, 124111.
- (47) Thomas, N.; Smidt, T.; Kearnes, S.; Yang, L.; Li, L.; Kohlhoff, K.; Riley, P. Tensor field networks: Rotation- and translation-equivariant neural networks for 3D point clouds. *arXiv preprint* **2018**, arXiv:1802.08219.
- (48) Townshend, R. J.; Townshend, B.; Eismann, S.; Dror, R. O. Geometric prediction: Moving beyond scalars. *arXiv preprint* **2020**, arXiv:2006.14163.
- (49) Anderson, B.; Hy, T. S.; Kondor, R. Cormorant: Covariant molecular neural networks. *Adv. Neural Inf. Process. Syst.* **2019**, *32*, 14537–14546.
- (50) Satorras, V. G.; Hoogeboom, E.; Welling, M. E(n) equivariant graph neural networks.

Proceedings of the 38th International Conference on Machine Learning. 2021; pp 9323–9332.

- (51) Christensen, A. S.; Sirumalla, S. K.; Qiao, Z.; O’Connor, M. B.; Smith, D. G.; Ding, F.; Bygrave, P. J.; Anandkumar, A.; Welborn, M.; Manby, F. R. et al. OrbNet Denali: A machine learning potential for biological and organic chemistry with semi-empirical cost and DFT accuracy. *J. Chem. Phys.* **2021**, *155*, 204103.
- (52) Schütt, K.; Unke, O.; Gastegger, M. Equivariant message passing for the prediction of tensorial properties and molecular spectra. Proceedings of the 38th International Conference on Machine Learning. 2021; pp 9377–9388.
- (53) Unke, O. T.; Chmiela, S.; Gastegger, M.; Schütt, K. T.; Sauceda, H. E.; Müller, K.-R. SpookyNet: Learning force fields with electronic degrees of freedom and nonlocal effects. *Nat. Commun.* **2021**, *12*, 7273.
- (54) Zhang, Y.; Ye, S.; Zhang, J.; Hu, C.; Jiang, J.; Jiang, B. Efficient and accurate simulations of vibrational and electronic spectra with symmetry-preserving neural network models for tensorial properties. *J. Phys. Chem. B* **2020**, *124*, 7284–7290.
- (55) Nguyen, V. H. A.; Lunghi, A. Predicting tensorial molecular properties with equivariant machine learning models. *Phys. Rev. B* **2022**, *105*, 165131.
- (56) Batatia, I.; Kovacs, D. P.; Simm, G.; Ortner, C.; Csanyi, G. MACE: Higher order equivariant message passing neural networks for fast and accurate force fields. *Adv. Neural Inf. Process. Syst.* **2022**, *35*, 11423–11436.
- (57) Liao, Y.-L.; Smidt, T. Equiformer: Equivariant graph attention transformer for 3D atomistic graphs. *arXiv preprint* **2022**, arXiv:2206.11990.
- (58) Fuchs, F.; Worrall, D.; Fischer, V.; Welling, M. SE(3)-Transformers: 3D roto-

- translation equivariant attention networks. *Adv. Neural Inf. Process. Syst.* **2020**, *33*, 1970–1981.
- (59) Simeon, G.; De Fabritiis, G. TensorNet: Cartesian tensor representations for efficient learning of molecular potentials. *Adv. Neural Inf. Process. Syst.* **2023**, *36*, 37334–37353.
- (60) Corso, G.; Stark, H.; Jegelka, S.; Jaakkola, T.; Barzilay, R. Graph neural networks. *Nat. Rev. Methods Primers* **2024**, *4*, 17.
- (61) Duval, A.; Mathis, S. V.; Joshi, C. K.; Schmidt, V.; Miret, S.; Malliaros, F. D.; Cohen, T.; Liò, P.; Bengio, Y.; Bronstein, M. A hitchhiker’s guide to geometric GNNs for 3D atomic systems. *arXiv preprint* **2023**, arXiv:2312.07511.
- (62) Musaelian, A.; Batzner, S.; Johansson, A.; Sun, L.; Owen, C. J.; Kornbluth, M.; Kozinsky, B. Learning local equivariant representations for large-scale atomistic dynamics. *Nat. Commun.* **2023**, *14*, 579.
- (63) Wen, M.; Horton, M. K.; Munro, J. M.; Huck, P.; Persson, K. A. An equivariant graph neural network for the elasticity tensors of all seven crystal systems. *Digital Discovery* **2024**, *3*, 869–882.
- (64) Batatia, I.; Batzner, S.; Kovács, D. P.; Musaelian, A.; Simm, G. N. C.; Drautz, R.; Ortner, C.; Kozinsky, B.; Csányi, G. The design space of E(3)-equivariant atom-centered interatomic potentials. *arXiv preprint* **2022**, arXiv:2205.06643.
- (65) Liu, Y.; Wang, L.; Liu, M.; Zhang, X.; Oztekin, B.; Ji, S. Spherical message passing for 3D graph networks. *arXiv preprint* **2022**, arXiv:2102.05013.
- (66) Kondor, R. *N*-body networks: A covariant hierarchical neural network architecture for learning atomic potentials. *arXiv preprint* **2018**, arXiv:1803.01588.

- (67) Bochkarev, A.; Lysogorskiy, Y.; Ortner, C.; Csányi, G.; Drautz, R. Multilayer atomic cluster expansion for semilocal interactions. *Phys. Rev. Res.* **2022**, *4*, L042019.
- (68) Lewis-Atwell, T.; Townsend, P. A.; Grayson, M. N. Machine learning activation energies of chemical reactions. *WIREs Comput. Mol. Sci.* **2022**, *12*, e1593.
- (69) Gallarati, S.; Fabregat, R.; Laplaza, R.; Bhattacharjee, S.; Wodrich, M. D.; Corminboeuf, C. Reaction-based machine learning representations for predicting the enantioselectivity of organocatalysts. *Chem. Sci.* **2021**, *12*, 6879–6889.
- (70) Grambow, C. A.; Pattanaik, L.; Green, W. H. Deep learning of activation energies. *J. Phys. Chem. Lett.* **2020**, *11*, 2992–2997.
- (71) Heid, E.; Green, W. H. Machine learning of reaction properties via learned representations of the condensed graph of reaction. *J. Chem. Inf. Model.* **2022**, *62*, 2101–2110.
- (72) Spiekermann, K. A.; Pattanaik, L.; Green, W. H. Fast predictions of reaction barrier heights: Toward coupled-cluster accuracy. *J. Phys. Chem. A* **2022**, *126*, 3976–3986.
- (73) Zhao, Q.; Anstine, D. M.; Isayev, O.; Savoie, B. M. Δ^2 machine learning for reaction property prediction. *Chem. Sci.* **2023**, *14*, 13392–13401.
- (74) Heinen, S.; von Rudorff, G. F.; von Lilienfeld, O. A. Toward the design of chemical reactions: Machine learning barriers of competing mechanisms in reactant space. *J. Chem. Phys.* **2021**, *155*, 064105.
- (75) Singh, A. R.; Rohr, B. A.; Gauthier, J. A.; Nørskov, J. K. Predicting chemical reaction barriers with a machine learning model. *Catal. Lett.* **2019**, *149*, 2347–2354.
- (76) Choi, S.; Kim, Y.; Kim, J. W.; Kim, Z.; Kim, W. Y. Feasibility of activation energy prediction of gas-phase reactions by machine learning. *Chem. Eur. J.* **2018**, *24*, 12354–12358.

- (77) Farrar, E. H. E.; Grayson, M. N. Machine learning and semi-empirical calculations: A synergistic approach to rapid, accurate, and mechanism-based reaction barrier prediction. *Chem. Sci.* **2022**, *13*, 7594–7603.
- (78) Friederich, P.; dos Passos Gomes, G.; Bin, R. D.; Aspuru-Guzik, A.; Balcells, D. Machine learning dihydrogen activation in the chemical space surrounding Vaska’s complex. *Chem. Sci.* **2020**, *11*, 4584–4601.
- (79) Migliaro, I.; Cundari, T. R. Density functional study of methane activation by frustrated lewis pairs with group 13 trihalides and group 15 pentahalides and a machine learning analysis of their barrier heights. *J. Chem. Inf. Model.* **2020**, *60*, 4958–4966.
- (80) Lewis-Atwell, T.; Beechey, D.; Şimşek, Ö.; Grayson, M. N. Reformulating reactivity design for data-efficient machine learning. *ACS Catal.* **2023**, *13*, 13506–13515.
- (81) Vadaddi, S. M.; Zhao, Q.; Savoie, B. M. Graph to activation energy models easily reach irreducible errors but show limited transferability. *J. Phys. Chem. A* **2024**, *128*, 2543–2555.
- (82) Ramos, J. E. A.; Neeser, R. M. M.; Stuyver, T. Repurposing quantum chemical descriptor datasets for on-the-fly generation of informative reaction representations: Application to hydrogen atom transfer reactions. *Digital Discovery* **2024**, *3*, 919–931.
- (83) Schwaller, P.; Vaucher, A. C.; Laplaza, R.; Bunne, C.; Krause, A.; Corminboeuf, C.; Laino, T. Machine intelligence for chemical reaction space. *WIREs Comput. Mol. Sci.* **2022**, *12*, e1604.
- (84) Rogers, D.; Hahn, M. Extended-connectivity fingerprints. *J. Chem. Inf. Model.* **2010**, *50*, 742–754.
- (85) Probst, D.; Schwaller, P.; Reymond, J.-L. Reaction classification and yield prediction using the differential reaction fingerprint DRFP. *Digital Discovery* **2022**, *1*, 91–97.

- (86) Ahneman, D. T.; Estrada, J. G.; Lin, S.; Dreher, S. D.; Doyle, A. G. Predicting reaction performance in C–N cross-coupling using machine learning. *Science* **2018**, *360*, 186–190.
- (87) Żurański, A. M.; Martínez Alvarado, J. I.; Shields, B. J.; Doyle, A. G. Predicting reaction yields via supervised learning. *Acc. Chem. Res.* **2021**, *54*, 1856–1865.
- (88) Zahrt, A. F.; Henle, J. J.; Rose, B. T.; Wang, Y.; Darrow, W. T.; Denmark, S. E. Prediction of higher-selectivity catalysts by computer-driven workflow and machine learning. *Science* **2019**, *363*, eaau5631.
- (89) Jorner, K.; Brinck, T.; Norrby, P.-O.; Buttar, D. Machine learning meets mechanistic modelling for accurate prediction of experimental activation energies. *Chem. Sci.* **2021**, *12*, 1163–1175.
- (90) Reid, J. P.; Sigman, M. S. Holistic prediction of enantioselectivity in asymmetric catalysis. *Nature* **2019**, *571*, 343–348.
- (91) Gensch, T.; dos Passos Gomes, G.; Friederich, P.; Peters, E.; Gaudin, T.; Pollice, R.; Jorner, K.; Nigam, A.; Lindner-D’Addario, M.; Sigman, M. S. et al. A comprehensive discovery platform for organophosphorus ligands for catalysis. *J. Am. Chem. Soc.* **2022**, *144*, 1205–1217.
- (92) Santiago, C. B.; Guo, J.-Y.; Sigman, M. S. Predictive and mechanistic multivariate linear regression models for reaction development. *Chem. Sci.* **2018**, *9*, 2398–2412.
- (93) Jorner, K. Putting chemical knowledge to work in machine learning for reactivity. *Chimia* **2023**, *77*, 22.
- (94) Gallegos, L. C.; Luchini, G.; St. John, P. C.; Kim, S.; Paton, R. S. Importance of engineered and learned molecular representations in predicting organic reactivity, selectivity, and chemical properties. *Acc. Chem. Res.* **2021**, *54*, 827–836.

- (95) Williams, W. L.; Zeng, L.; Gensch, T.; Sigman, M. S.; Doyle, A. G.; Anslyn, E. V. The evolution of data-driven modeling in organic chemistry. *ACS Cent. Sci.* **2021**, *7*, 1622–1637.
- (96) Stuyver, T.; Coley, C. W. Machine learning-guided computational screening of new candidate reactions with high bioorthogonal click potential. *Chem. Eur. J.* **2023**, *29*, e202300387.
- (97) Stuyver, T.; Coley, C. W. Quantum chemistry-augmented neural networks for reactivity prediction: Performance, generalizability, and explainability. *J. Chem. Phys.* **2022**, *156*, 084104.
- (98) Vargas, S.; Gee, W.; Alexandrova, A. High-throughput quantum theory of atoms in molecules (QTAIM) for geometric deep learning of molecular and reaction properties. *Digital Discovery* **2024**, *3*, 987–998.
- (99) Vijay, S.; Venetos, M. C.; Spotte-Smith, E. W. C.; Kaplan, A. D.; Wen, M.; Persson, K. A. CoeffNet: Predicting activation barriers through a chemically-interpretable, equivariant and physically constrained graph neural network. *Chem. Sci.* **2024**, *15*, 2923–2936.
- (100) Devlin, J.; Chang, M.-W.; Lee, K.; Toutanova, K. Bert: Pre-training of deep bidirectional transformers for language understanding. *arXiv preprint* **2018**, arXiv:1810.04805.
- (101) Schwaller, P.; Laino, T.; Gaudin, T.; Bolgar, P.; Hunter, C. A.; Bekas, C.; Lee, A. A. Molecular transformer: A model for uncertainty-calibrated chemical reaction prediction. *ACS Cent. Sci.* **2019**, *5*, 1572–1583.
- (102) Schwaller, P.; Vaucher, A. C.; Laino, T.; Reymond, J.-L. Prediction of chemical reaction yields using deep learning. *Mach. Learn.: Sci. Technol.* **2021**, *2*, 015016.

- (103) Heid, E.; Greenman, K. P.; Chung, Y.; Li, S.-C.; Graff, D. E.; Vermeire, F. H.; Wu, H.; Green, W. H.; McGill, C. J. Chemprop: A machine learning package for chemical property prediction. *J. Chem. Inf. Model.* **2024**, *64*, 9–17.
- (104) Chen, W. L.; Chen, D. Z.; Taylor, K. T. Automatic reaction mapping and reaction center detection. *WIREs Comput. Mol. Sci.* **2013**, *3*, 560–593.
- (105) Preciat Gonzalez, G. A.; El Assal, L. R.; Noronha, A.; Thiele, I.; Haraldsdóttir, H. S.; Fleming, R. M. Comparative evaluation of atom mapping algorithms for balanced metabolic reactions: Application to Recon 3D. *J. Cheminform.* **2017**, *9*, 39.
- (106) Jaworski, W.; Szymkuć, S.; Mikulak-Klucznik, B.; Piecuch, K.; Klucznik, T.; Kaźmierowski, M.; Rydzewski, J.; Gambin, A.; Grzybowski, B. A. Automatic mapping of atoms across both simple and complex chemical reactions. *Nat. Commun.* **2019**, *10*, 1434.
- (107) Schwaller, P.; Hoover, B.; Reymond, J.-L.; Strobelt, H.; Laino, T. Extraction of organic chemistry grammar from unsupervised learning of chemical reactions. *Sci. Adv.* **2021**, *7*, eabe4166.
- (108) Doney, A. C.; Rooks, B. J.; Lu, T.; Wheeler, S. E. Design of organocatalysts for asymmetric propargylations through computational screening. *ACS Catal.* **2016**, *6*, 7948–7955.
- (109) Nehil-Puleo, K.; Quach, C. D.; Craven, N. C.; McCabe, C.; Cummings, P. T. E(*n*) equivariant graph neural network for learning interactional properties of molecules. *J. Phys. Chem. B* **2024**, *128*, 1108–1117.
- (110) Duan, C.; Du, Y.; Jia, H.; Kulik, H. J. Accurate transition state generation with an object-aware equivariant elementary reaction diffusion model. *arXiv preprint* **2023**, arXiv:2304.06174.

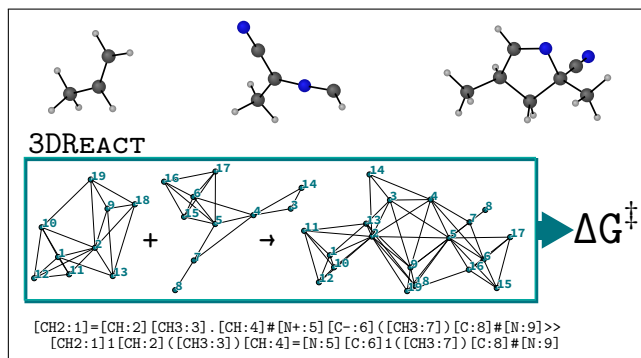
- (111) Zhang, J.; Lei, Y.-K.; Zhang, Z.; Han, X.; Li, M.; Yang, L.; Yang, Y. I.; Gao, Y. Q. Deep reinforcement learning of transition states. *Phys. Chem. Chem. Phys.* **2021**, *23*, 6888–6895.
- (112) Pattanaik, L.; Ingraham, J. B.; Grambow, C. A.; Green, W. H. Generating transition states of isomerization reactions with deep learning. *Phys. Chem. Chem. Phys.* **2020**, *22*, 23618–23626.
- (113) Makoś, M. Z.; Verma, N.; Larson, E. C.; Freindorf, M.; Kraka, E. Generative adversarial networks for transition state geometry prediction. *J. Chem. Phys.* **2021**, *155*, 024116.
- (114) Kim, S.; Woo, J.; Kim, W. Y. Diffusion-based generative AI for exploring transition states from 2D molecular graphs. *Nat. Commun.* **2024**, *15*, 341.
- (115) Choi, S. Prediction of transition state structures of gas-phase chemical reactions via machine learning. *Nat. Commun.* **2023**, *14*, 1168.
- (116) Spiekermann, K.; Pattanaik, L.; Green, W. H. High accuracy barrier heights, enthalpies, and rate coefficients for chemical reactions. *Sci. Data* **2022**, *9*, 417.
- (117) Stuyver, T.; Jorner, K.; Coley, C. W. Reaction profiles for quantum chemistry-computed [3 + 2] cycloaddition reactions. *Sci. Data* **2023**, *10*, 66.
- (118) Geiger, M.; Smidt, T.; M., A.; Miller, B. K.; Boomsma, W.; Dice, B.; Lapchevskiy, K.; Weiler, M.; Tyszkiewicz, M.; Uhrin, M. et al. e3nn/e3nn: 2022-12-12. 2022; <https://zenodo.org/records/7430260>.
- (119) Corso, G.; Stärk, H.; Jing, B.; Barzilay, R.; Jaakkola, T. DiffDock: Diffusion steps, twists, and turns for molecular docking. *arXiv preprint* **2023**, arXiv:2210.01776.
- (120) Landrum, G.; Tosco, P.; Kelley, B.; Ric, S.; Sriniker, S.; Cosgrove, D.; Gedeck, J.; Vianello, R.;

- NadineSchneider,; Kawashima, E. et al. rdkit/rdkit: 2023_03_1 (Q1 2023) release. 2023; <https://zenodo.org/record/7880616>.
- (121) Stärk, H.; Ganea, O.; Pattanaik, L.; Barzilay, R.; Jaakkola, T. EquiBind: Geometric deep learning for drug binding structure prediction. Proceedings of the 39th International Conference on Machine Learning. 2022; pp 20503–20521.
- (122) Ganea, O.-E.; Huang, X.; Bunne, C.; Bian, Y.; Barzilay, R.; Jaakkola, T.; Krause, A. Independent SE(3)-equivariant models for end-to-end rigid protein docking. *arXiv preprint* **2022**, arXiv:2111.07786.
- (123) Grambow, C.; Pattanaik, L.; Green, W. Reactants, products, and transition states of elementary chemical reactions based on quantum chemistry. *Sci. Data* **2020**, *7*, 137.
- (124) van Gerwen, P.; Wodrich, M. D.; Laplaza, R.; Corminboeuf, C. Reply to Comment on ‘Physics-based representations for machine learning properties of chemical reactions’. *Mach. Learn.: Sci. Technol.* **2023**, *4*, 048002.
- (125) Lowe, D. M. Extraction of chemical structures and reactions from the literature. Ph.D. thesis, University of Cambridge, 2012.
- (126) von Lilienfeld, O. A. First principles view on chemical compound space: Gaining rigorous atomistic control of molecular properties. *Int. J. Quantum Chem.* **2013**, *113*, 1676–1689.
- (127) Bemis, G. W.; Murcko, M. A. The properties of known drugs. 1. Molecular frameworks. *J. Med. Chem.* **1996**, *39*, 2887–2893.
- (128) van der Maaten, L.; Hinton, G. Visualizing data using t-SNE. *J. Mach. Learn. Res.* **2008**, *9*, 2579–2605.
- (129) Bannwarth, C.; Ehlert, S.; Grimme, S. GFN2-xTB—An accurate and broadly parametrized self-consistent tight-binding quantum chemical method with multipole

- electrostatics and density-dependent dispersion contributions. *J. Chem. Theory Comput.* **2019**, *15*, 1652–1671.
- (130) Blum, L. C.; Reymond, J.-L. 970 million druglike small molecules for virtual screening in the chemical universe database GDB-13. *J. Am. Chem. Soc.* **2009**, *131*, 8732–8733.
- (131) Reymond, J.-L. The chemical space project. *Acc. Chem. Res.* **2015**, *48*, 722–730.
- (132) Ramakrishnan, R.; Dral, P. O.; Rupp, M.; von Lilienfeld, O. A. Quantum chemistry structures and properties of 134 kilo molecules. *Sci. Data* **2014**, *1*, 140022.
- (133) Zimmerman, P. M. Single-ended transition state finding with the growing string method. *J. Comput. Chem.* **2015**, *36*, 601–611.
- (134) Cordella, L. P.; Foggia, P.; Sansone, C.; Vento, M. An improved algorithm for matching large graphs. 3rd IAPR-TC15 workshop on graph-based representations in pattern recognition. 2001; pp 149–159.
- (135) Hagberg, A. A.; Schult, D. A.; Swart, P. J. Exploring network structure, dynamics, and function using NetworkX. Proceedings of the 7th Python in Science Conference. 2008; pp 11–15.
- (136) Wu, Z.; Ramsundar, B.; Feinberg, E. N.; Gomes, J.; Geniesse, C.; Pappu, A. S.; Leswing, K.; Pande, V. MoleculeNet: A benchmark for molecular machine learning. *Chem. Sci.* **2018**, *9*, 513–530.
- (137) Yang, K.; Swanson, K.; Jin, W.; Coley, C.; Eiden, P.; Gao, H.; Guzman-Perez, A.; Hopper, T.; Kelley, B.; Mathea, M. et al. Analyzing learned molecular representations for property prediction. *J. Chem. Inf. Model.* **2019**, *59*, 3370–3388.
- (138) Riniker, S.; Landrum, G. A. Better informed distance geometry: Using what we know to improve conformation generation. *J. Chem. Inf. Model.* **2015**, *55*, 2562–2574.

- (139) Tosco, P.; Stiefl, N.; Landrum, G. Bringing the MMFF force field to the RDKit: implementation and validation. *J. Cheminform.* **2014**, *6*, 37.
- (140) Atkinson, P.; Bannwarth, C.; Bohle, F.; Brandenburg, G.; Caldeweyher, E.; Chęcinski, M.; Dohm, S.; Ehlert, S.; Ehrlich, S.; Gerasimov, I. et al. Semiempirical Extended Tight-Binding Program Package. <https://github.com/grimme-lab/xtb>, 2019.
- (141) Kingma, D. P.; Ba, J. Adam: A method for stochastic optimization. *arXiv preprint* **2014**, arXiv:1412.6980.
- (142) Biewald, L. Experiment Tracking with Weights and Biases. 2020; <https://www.wandb.com/>, Software available from wandb.com.
- (143) Christensen, A. S.; Faber, F.; Huang, B.; Bratholm, L.; Tkatchenko, A.; Müller, K.-R.; von Lilienfeld, O. A. QML: A Python toolkit for quantum machine learning. <https://github.com/qmlcode/qml>, 2017.

TOC Graphic



SUPPLEMENTARY INFORMATION

3DReact: Geometric deep learning for chemical reactions

Puck van Gerwen,^{1,2} Ksenia R. Briling,^{2,3} Charlotte Bunne,^{2,3} Vignesh Ram Somnath,^{2,3} Ruben Laplaza,^{1,2} Andreas Krause,^{2,3} and Clemence Corminboeuf^{1,2, a)}

¹⁾ *Laboratory for Computational Molecular Design, Institute of Chemical Sciences and Engineering, École Polytechnique Fédérale de Lausanne, 1015 Lausanne, Switzerland*

²⁾ *National Center for Competence in Research – Catalysis (NCCR-Catalysis), École Polytechnique Fédérale de Lausanne, 1015 Lausanne, Switzerland*

³⁾ *Learning & Adaptive Systems Group, Department of Computer Science, ETH Zurich, 8092 Zurich, Switzerland*

(Dated: 15 July 2024)

CONTENTS

S1. Molecular channels	S2
S2. Model hyperparameters	S4
S3. Root-mean-square errors	S5
S4. Cross-attention as a surrogate for atom-mapping in the “None” regime	S6
S5. Extrapolation studies	S7
S6. Correlation plots for the GDB7-22-TS dataset	S9
S7. Performance with and without explicit hydrogen atoms	S9
S8. Geometry sensitivity for the Cyclo-23-TS dataset	S12
References	S13

^{a)} Electronic mail: clemence.corminboeuf@epfl.ch

S1. MOLECULAR CHANNELS

As briefly described in the main text, a molecule is represented as a distance-based graph where nodes describe atoms and edges describe bonds. Instead of explicitly using connectivity information, the ‘‘bonds’’ of atom a are formed with all the neighboring $\text{Neigh}(a)$ atoms within the cutoff r_{\max} , all the (directed) bonds $\{(a, b)\}$ in the molecule forming set \mathfrak{B} . Initial node (atom) features $\{\mathbf{x}_a^{(0)}\}$ encode several cheminformatic features from `RDKit`,^{S1} including atomic number, chirality tag (unspecified, tetrahedral, or other, including octahedral, square planar, allene-type, *etc.*), number of directly-bonded neighbors, number of rings, implicit valence, formal charge, number of attached hydrogens, number of radical electrons, hybridization, aromaticity, presence in rings of specified sizes from 3 to 7.

Inspired from related models,^{S2} initial scalar edge (bond) features $\{\mathbf{e}_{ab}^{(0)}\}$ are projections of the atom distances $|\mathbf{r}_{ab}|$ onto n_g Gaussians uniformly spanning the line segment from 0 to r_{\max} with the step $\Delta\mu = r_{\max}/(n_g - 1)$,

$$\mathbf{e}_{ab}^{(0)} = \mathbf{f}_1(|\mathbf{r}_{ab}|) \quad \forall (a, b) \in \mathfrak{B}, \quad (\text{S1})$$

$$\mathbf{f}_1(r) = \left\{ \exp\left(-\frac{1}{2}\left(\frac{r - n\Delta\mu}{\Delta\mu}\right)^2\right) \right\} \quad n \in 0, \dots, n_g - 1. \quad (\text{S2})$$

The tensorial edge features $\{\mathbf{z}_{ab}\}$, later used as filters, are projections of normalized difference vectors between atomic positions $\mathbf{r}_{ab}/|\mathbf{r}_{ab}|$ onto spherical harmonics Y_m^ℓ of $0 \leq \ell \leq 2$,

$$\mathbf{z}_{ab} \equiv \mathbf{z}_{ab}^{0e} \oplus \mathbf{z}_{ab}^{1o} \oplus \mathbf{z}_{ab}^{2e} = \mathbf{f}_2(\mathbf{r}_{ab}/|\mathbf{r}_{ab}|) \quad \forall (a, b) \in \mathfrak{B}, \quad (\text{S3})$$

$$\mathbf{f}_2(\mathbf{r}) = Y_0^0(\mathbf{r}) \oplus \{Y_m^1(\mathbf{r})\}_{|m| \leq 1} \oplus \{Y_m^2(\mathbf{r})\}_{|m| \leq 2}, \quad (\text{S4})$$

where \oplus denotes the concatenation operator, and the components of \mathbf{z}_{ab} are labelled in superscript by the corresponding irreducible representation (ℓe for even parity and ℓo for odd parity) of the $O(3)$ group.^{S3} The initial $\mathbf{x}^{(0)}$ and $\mathbf{e}^{(0)}$ are then passed through embeddings to give $\mathbf{x}_a^{(1)} \forall a$ and $\mathbf{e}_{ab} \forall (a, b) \in \mathfrak{B}$.

The atomic representations $\{\mathbf{x}_a^{(1)}\}$ are updated by $n_{\text{conv}} \in \{2, 3\}$ equivariant convolutional layers:

$$\text{Layer 1} \left\{ \begin{array}{l} \mathbf{w}_{ab}^{(1)} = \mathbf{g}_{31}(\mathbf{e}_{ab} \oplus \mathbf{x}_a^{(1)} \oplus \mathbf{x}_b^{(1)}) \quad \forall (a, b) \in \mathfrak{B} \\ \mathbf{s}_b^{(1)} \equiv \mathbf{s}_b^{0e(1)} \oplus \mathbf{s}_b^{1o(1)} \end{array} \right. \quad (\text{S5})$$

$$= \frac{1}{\text{Neigh}(b)} \sum_{a:(a,b) \in \mathfrak{B}} \mathbf{t}_1(\mathbf{x}_a^{(1)}, \mathbf{z}_{ab}, \mathbf{w}_{ab}^{(1)}) \quad \forall b \quad (\text{S6})$$

$$\mathbf{x}^{0e(2)} = \mathbf{x}^{(1)} + \mathbf{s}^{0e(1)} \quad (\text{S7})$$

$$\mathbf{x}^{(2)} = \mathbf{x}^{0e(2)} \oplus \mathbf{s}^{1o(1)} \quad (\text{S8})$$

$$\text{Layer 2} \left\{ \begin{array}{l} \mathbf{w}_{ab}^{(2)} = \mathbf{g}_{32}(\mathbf{e}_{ab} \oplus \mathbf{x}_a^{0e(2)} \oplus \mathbf{x}_b^{0e(2)}) \quad \forall (a, b) \in \mathfrak{B} \\ \mathbf{s}_b^{(2)} \equiv \mathbf{s}_b^{0e(2)} \oplus \mathbf{s}_b^{1o(2)} \oplus \mathbf{s}_b^{1e(2)} \end{array} \right. \quad (\text{S9})$$

$$= \frac{1}{\text{Neigh}(b)} \sum_{a:(a,b) \in \mathfrak{B}} \mathbf{t}_2(\mathbf{x}_a^{(2)}, \mathbf{z}_{ab}, \mathbf{w}_{ab}^{(2)}) \quad \forall b \quad (\text{S10})$$

$$\mathbf{x}^{0e(3)} = \mathbf{x}^{0e(2)} + \mathbf{s}^{0e(2)} \quad (\text{S11})$$

$$\mathbf{x}^{(3)} = \mathbf{x}^{0e(3)} \oplus (\mathbf{s}^{1o(1)} + \mathbf{s}^{1o(2)}) \oplus \mathbf{s}^{1e(2)} \quad (\text{S12})$$

$$\text{Layer 3} \left\{ \begin{array}{l} \mathbf{w}_{ab}^{(3)} = \mathbf{g}_{33}(\mathbf{e}_{ab} \oplus \mathbf{x}_a^{0e(3)} \oplus \mathbf{x}_b^{0e(3)}) \quad \forall (a, b) \in \mathfrak{B} \\ \mathbf{s}_b^{(3)} \equiv \mathbf{s}_b^{0e(3)} \oplus \mathbf{s}_b^{1o(3)} \oplus \mathbf{s}_b^{1e(3)} \oplus \mathbf{s}_b^{0o(3)} \end{array} \right. \quad (\text{S13})$$

$$= \frac{1}{\text{Neigh}(b)} \sum_{a:(a,b) \in \mathfrak{B}} \mathbf{t}_3(\mathbf{x}_a^{(3)}, \mathbf{z}_{ab}, \mathbf{w}_{ab}^{(3)}) \quad \forall b \quad (\text{S14})$$

$$\mathbf{x}^{\text{out}} = (\mathbf{x}^{0e(3)} + \mathbf{s}^{0e(3)}) \oplus \mathbf{s}^{0o(3)}. \quad (\text{S15})$$

In **Layer 1**, for example, $\mathbf{s}_b^{(1)} \equiv \mathbf{s}_b^{0e(1)} \oplus \mathbf{s}_b^{1o(1)}$ means that the result of the function \mathbf{t}_1 consists of scalars (0e) and vectors (1o) that can be treated separately. Each function $\mathbf{t}_n(\mathbf{x}, \mathbf{z}, \mathbf{w})$ is a fully-connected weighted tensor product,

as defined in `e3nn`,^{S4} in the form of

$$\mathbf{t}_n(\mathbf{x}, \mathbf{z}, \mathbf{w}) = \bigoplus_k \mathbf{t}_k^{(n)}, \quad \mathbf{t}_k^{(n)} = \sum_{uv} w_{uvk}^{(n)} \mathbf{x}_u \otimes \mathbf{z}_v, \quad (\text{S16})$$

where $\{k, u, v\}$ index individual tensors. Note that a tensor here refers to the mathematical object that obeys certain transformation laws, not the multi-dimensional array. The functions $\{\mathbf{t}_n\}$ are specified by signatures of irreducible representations (irreps) of two input and one output $O(3)$ tensors. The output tensor is a combination of weighted sums of paths (pairs of input irreps) leading to each output irrep. The irreducible representation (irrep) sequence in each layer from 1–3 is illustrated in Figure S1,

For example, irreps of $\mathbf{x}_a^{(0)}$ and \mathbf{z}_{ab} are $(n_s \times 0e)$ and $(0e \oplus 1o \oplus 2e)$, respectively, because the former consists of n_s scalars and the latter is a direct sum of projections onto spherical harmonics of $\ell = 0, 1, 2$. The desired output irreps are chosen deliberately from the possible products of the input irreps and can have any shape, so the signature of function \mathbf{t}_1 is

$$\mathbf{t}_1 : (n_s \times 0e) \otimes (0e \oplus 1o \oplus 2e) \rightarrow (n_s \times 0e \oplus n_v \times 1o). \quad (\text{S17})$$

Thus two paths are created,

$$(n_s \times 0e) \otimes (1 \times 0e) \rightarrow (n_s \times 0e) \quad \text{with } n_s \times 1 \times n_s \text{ weights}, \quad (\text{S18})$$

$$(n_s \times 0e) \otimes (1 \times 1o) \rightarrow (n_v \times 1o) \quad \text{with } n_s \times 1 \times n_v \text{ weights}. \quad (\text{S19})$$

The output contains n_s scalars and n_v vectors. There is one tensor per each bond (a, b) , so a tensor $\mathbf{s}_b^{(1)}$ for atom b is an average of $\mathbf{t}_1(\mathbf{x}_a^{(1)}, \mathbf{z}_{ab}, \mathbf{w}_{ab}^{(1)})$ over its neighbors $\{a\}$. It is used to update \mathbf{x} which is convoluted with \mathbf{z}_a two more times using functions with signatures

$$\mathbf{t}_2 : (n_s \times 0e \oplus n_v \times 1o) \otimes (0e \oplus 1o \oplus 2e) \rightarrow (n_s \times 0e \oplus n_v \times 1o \oplus n_v \times 1e), \quad (\text{S20})$$

adding n_v pseudovectors ($n_s^2 + 2n_s n_v + 3n_v^2$ weights total), and

$$\mathbf{t}_3 : (n_s \times 0e \oplus n_v \times 1o \oplus n_v \times 1e) \otimes (0e \oplus 1o \oplus 2e) \rightarrow (n_s \times 0e \oplus n_v \times 1o \oplus n_v \times 1e \oplus n_s \times 0o), \quad (\text{S21})$$

adding n_s pseudoscalars ($n_s^2 + 3n_s n_v + 6n_v^2$ weights total).

To obtain the weights $\mathbf{w}^{(n)}$ for each convolutional layer n , the spherical parts of $\mathbf{x}_a^{(n)}$ and $\mathbf{x}_b^{(n)}$ are concatenated with the bond features \mathbf{e}_{ab} and passed through a multi-layer perceptron \mathbf{g}_{3n} .

The output of the equivariant molecular channels is the local molecular representation $\mathbf{X} \in \mathbb{R}^{N_{\text{at}} \times D}$ corresponding to N_{at} atoms associated with D features. Depending on the `sum_mode` hyperparameter, it is constructed either from the node features $\{\mathbf{x}_a^{\text{out}}\}$ (`node mode`) or both node and edge features $\{\mathbf{x}_a^{\text{out}} \oplus \sum_{b:(a,b) \in \mathfrak{B}} \mathbf{e}_{ab}^{(0)}\}$ (`both mode`). In the case of $n_{\text{conv}} = 2$, the vectors $\{\mathbf{x}_a^{0e(3)}\}$ are taken to construct the molecular representation.

Note that even through the resulting node features \mathbf{X} should be invariant (with $n_{\text{conv}} = 2$) or equivariant (with $n_{\text{conv}} = 3$) with coordinate inversion, the chirality tag, if present in the SMILES, changes the initial node features $\{\mathbf{x}_a^{(0)}\}$ and may lead to different representations for two enantiomers.

Above is described the architecture of EQUIREACT, the equivariant option of 3DREACT. The invariant option (INREACT) is implemented as a simplified version of the latter: the spherical harmonics filters take only $\ell = 0$ (hence $\mathbf{z}_{ab} = 1 \forall (a, b) \in \mathfrak{B}$), the convolutional layers signatures become

$$\mathbf{t}'_n : (n_s \times 0e) \otimes (0e) \rightarrow (n_s \times 0e), \quad n \in \{1, 2, 3\}, \quad (\text{S22})$$

and Eq. S16 is simplified to a dot product

$$\mathbf{t}'_n(\mathbf{x}, \mathbf{z}, \mathbf{w}) \equiv \mathbf{t}'_n(\mathbf{x}, \mathbf{w}) = \bigoplus_k \mathbf{t}'_k^{(n)}, \quad \mathbf{t}'_k^{(n)} = \sum_u w_{uk}^{(n)} x_u. \quad (\text{S23})$$

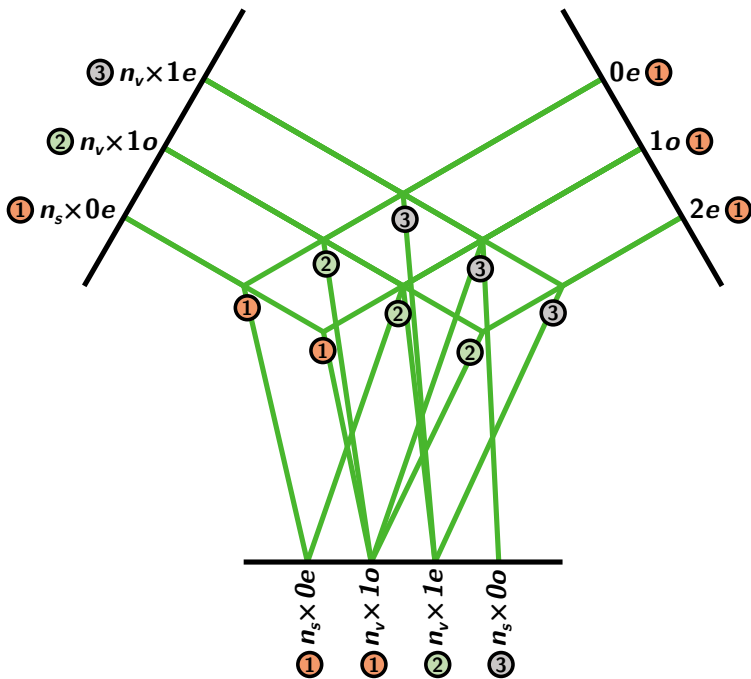


FIG. S1. Irrep sequence in the (1), (2), (3) convolutional layers of EQUIREACT. Input irreps are on the left (hidden atom and bond features) and right (spherical harmonics filters), output irreps are at the bottom, and paths that connect them are in the middle in green. Note that formally $2e$ is present in the right input already at the first layer, but does not contribute to the output.

S2. MODEL HYPERPARAMETERS

The best model hyperparameters obtained after the sweep on EQUIREACT are summarized in Table S1. These are the hyperparameters used in all 3DREACT models in the main text.

Parameter	GDB7-22-TS	Cyclo-23-TS	Proparg-21-TS
n_s	64	64	64
n_v	64	48	64
n_g	32	48	64
n_{conv}	2	2	3
$r_{\text{max}}, \text{\AA}$	2.5	2.5	5
n_{neigh}	10	50	10
p_d	0.05	0.1	0.05
sum_mode	both	node	node
combine_mode	diff	diff	diff
graph_mode	vector	energy	vector
learning rate	$5 \cdot 10^{-4}$	10^{-3}	10^{-3}
weight decay	10^{-5}	10^{-5}	10^{-5}

TABLE S1. Best model hyperparameters as a result of the sweeps.

S3. ROOT-MEAN-SQUARE ERRORS

The results presented in Table 2 and Table 1 are repeated in Table S2 using root mean squared errors (RMSEs) rather than mean absolute errors (MAEs) as the performance metric.

Dataset (property, units)	Atom-mapping regime	CHEMPROP	SLATM _d +KRR	INREACT	EQUIREACT
<i>Random splits</i>					
GDB7-22-TS (ΔE^\ddagger , kcal/mol)	True	7.6 ± 0.3	—	8.4 ± 0.4	8.4 ± 0.3
	RXNMapper	9.57 ± 0.28	—	9.9 ± 0.4	10.0 ± 0.4
	None	13.2 ± 0.5	10.8 ± 0.4	10.5 ± 0.4	10.4 ± 0.5
Cyclo-23-TS (ΔG^\ddagger , kcal/mol)	True	3.70 ± 0.20	—	3.33 ± 0.18	3.24 ± 0.21
	RXNMapper	3.72 ± 0.16	—	3.31 ± 0.21	3.29 ± 0.26
	None	3.73 ± 0.23	3.65 ± 0.22	3.34 ± 0.18	3.24 ± 0.23
Proparg-21-TS (ΔE^\ddagger , kcal/mol)	True	1.97 ± 0.16	—	0.58 ± 0.16	0.52 ± 0.14
	None	2.01 ± 0.19	0.52 ± 0.09	0.60 ± 0.16	0.49 ± 0.09
<i>Scaffold splits</i>					
GDB7-22-TS (ΔE^\ddagger , kcal/mol)	True	10.6 ± 0.9	—	11.6 ± 1.0	11.5 ± 1.2
	RXNMapper	12.8 ± 0.9	—	13.3 ± 1.0	13.3 ± 1.1
	None	17.4 ± 0.8	15.2 ± 1.3	14.5 ± 1.1	14.4 ± 1.1
Cyclo-23-TS (ΔG^\ddagger , kcal/mol)	True	3.9 ± 0.4	—	3.7 ± 0.4	3.7 ± 0.4
	RXNMapper	3.9 ± 0.4	—	3.7 ± 0.4	3.7 ± 0.5
	None	4.1 ± 0.4	4.0 ± 0.4	3.7 ± 0.4	3.7 ± 0.4
Proparg-21-TS (ΔE^\ddagger , kcal/mol)	True	2.2 ± 0.3	—	0.71 ± 0.22	0.65 ± 0.17
	None	2.2 ± 0.4	0.62 ± 0.16	0.68 ± 0.18	0.64 ± 0.19

TABLE S2. Performance as measured in root-mean-square errors (RMSEs) of predictions of 3DREACT (INREACT and EQUIREACT) vs. CHEMPROP and SLATM_d. 3DREACT_M is used for the “True” and “RXNMapper” regimes, and 3DREACT_S is used for the “None” regime. RMSEs are averaged over 10 folds of random/scaffold 80/10/10 splits (training/validation/test) and reported together with standard deviations across folds.

S4. CROSS-ATTENTION AS A SURROGATE FOR ATOM-MAPPING IN THE “NONE” REGIME

Since the “True” atom-mapping regime allowed for a significantly improved model over the “RXNMapper” and “None” regimes for the GDB7-22-TS dataset, we thought that a model based on cross-attention between reactants and products (3DREACT_X) could provide a competitive surrogate to the atom-mapping-based models.

Given queries $\mathbf{Q} \in \mathbb{R}^{N \times D}$, keys $\mathbf{K} \in \mathbb{R}^{M \times D}$ and values $\mathbf{V} \in \mathbb{R}^{M \times D}$, attention is computed as

$$\mathbf{A} = \text{softmax} \left(\frac{\mathbf{Q}\mathbf{K}^T}{\sqrt{D}} \right) \quad (\text{S24})$$

and the “reordered” values \mathbf{Y} are

$$\mathbf{Y} = \mathbf{A}\mathbf{V}. \quad (\text{S25})$$

We used the implementation of this scaled-dot-product attention^{S5} in PyTorch’s^{S6} `MultiheadAttention` (PyTorch version 1.12.1). The representations are re-ordered using Eq. S24 and Eq. S25 with \mathbf{Q} as the vector representation of reactants, \mathbf{K} and \mathbf{V} as the vector representations of products, and vice versa (thus here $N = M = N_{\text{at}}$).

However, we found that the cross-attention module does not improve over the simple model 3DREACT_S, based only on geometries of isolated reactants and products without any information exchange between them, for all three datasets (Table S3).

Dataset (property, units)	INREACT _X	INREACT _S	EQUIREACT _X	EQUIREACT _S
GDB7-22-TS (ΔE^\ddagger , kcal/mol)	6.68 ± 0.27	6.56 ± 0.26	6.7 ± 0.3	6.53 ± 0.28
Cyclo-23-TS (ΔG^\ddagger , kcal/mol)	2.53 ± 0.09	2.39 ± 0.05	2.43 ± 0.09	2.31 ± 0.09
Proparg-21-TS (ΔE^\ddagger , kcal/mol)	0.34 ± 0.05	0.34 ± 0.06	0.33 ± 0.06	0.31 ± 0.06

TABLE S3. Performance of the alternative models 3DREACT_X and 3DREACT_S in the None mapping mode.

Investigating further for the GDB7-22-TS dataset, we wanted to find out whether the attention module could infer atom-mapping from an easier, supervised learning scenario. The MAPPER model took the graphs of reactants and products as input, as for 3DREACT. Since the atom indices in the reactants were ordered sequentially (1, 2, 3, ...), the objective was to learn the permutation of the atom indices in the products, in order to map them to the reactants correctly. The true atom maps provided by the GDB7-22-TS set^{S7} were used to train and validate the model. The permutation was learned using cross-attention between atoms in reactants and products (Eq. S24) using queries \mathbf{Q} from the vector representation of reactants and keys \mathbf{K} from vector representations of products.

The model was trained using the Adam optimizer with default parameters. The hyperparameters used for the 3DREACT (EQUIREACT) components of the MAPPER model (to construct the molecular representations) are summarized in Table S4.

Parameter	n_s	n_v	n_g	n_{conv}	r_{max}	n_{neigh}	p_d
Value	16	16	32	2	10	20	0.1

TABLE S4. Hyperparameters used to construct molecular components in the MAPPER model.

The optimization objective was to minimize the cross-entropy loss between the true mapping permutation and the permutation learned by the model. MAPPER was run for 100 epochs on a single random 80/10/10 split of the GDB7-22-TS dataset. The resulting training and validation curves are shown in Figure S2.

While the model learns, both the training and validation accuracy saturate at around 70%, suggesting there is an upper bound to the accuracy of the MAPPER model. This may be related to the unconstrained nature of the optimization: while the predicted maps can converge to any integer value, each integer prediction should be taken from the pool of integers (atom-map labels) in the reactants, and appear only once. The architecture is also much simpler than that of RXNMAPPER^{S8} for example.

Nevertheless, the fact that the model is able to learn atom-mapping to a reasonable degree of accuracy suggests that the cross-attention module in 3DREACT could mimic a low-quality atom-mapping. Therefore, 3DREACT_X likely fails to improve model performance because the unsupervised atom-mapping task is embedded in a broader learning context. It seems that unlike the supervised task of reaction outcome prediction,^{S8} a graph-based model trained to predict reaction barriers does not learn chemical signatures like atom-mapping as part of the training process. Other information (like that based on the geometries of reactants and products) is instead exploited to make good predictions.

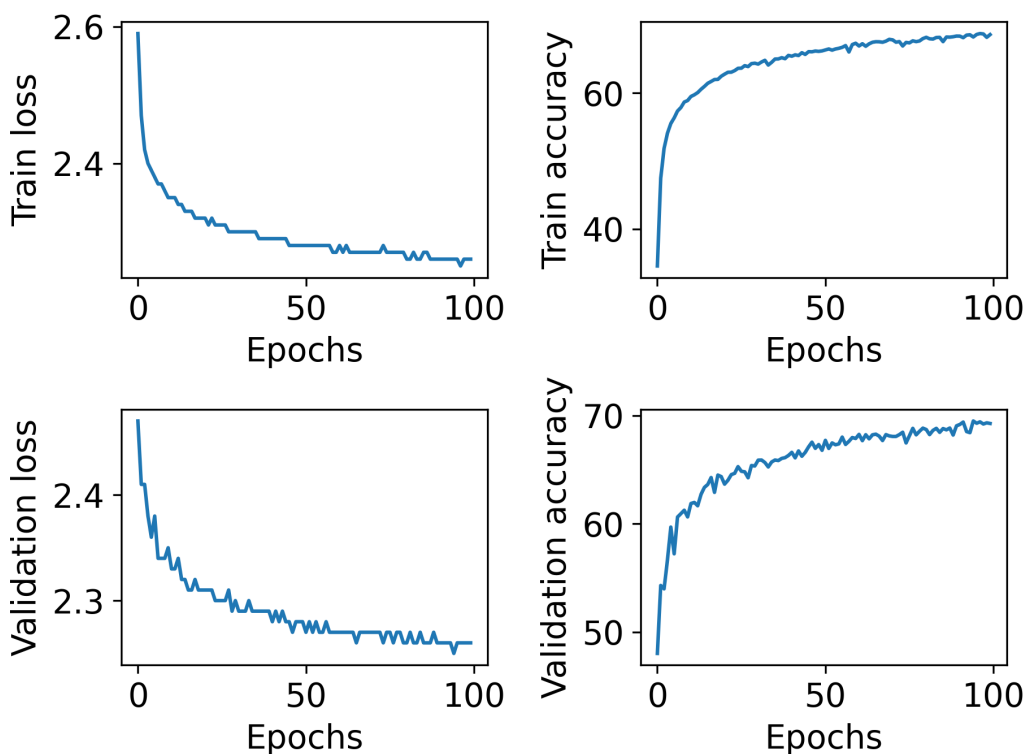


FIG. S2. Evolution of the training loss, training accuracy (%), validation loss, validation accuracy (%) for the MAPPER model, trained to learn atom-mapping in a supervised setting.

S5. EXTRAPOLATION STUDIES

Table S2 shows the results for an extensive set of extrapolation studies, both for INREACT and EQUIREACT as well as for the baseline models. Property-based splits order the training/validation/test sets according to the target value in ascending or descending order. The nonzero standard deviations for neural network models arise from different organization of the datapoints into batches. Size-based splits instead order the datapoints into training/validation/test sets according to molecular size, *i.e.*, number of heavy atoms (reactant size for GDB7-22-TS and Proparg-21-TS, product size for Cyclo-23-TS), again sorted in ascending or descending order. Since the molecular size is a discrete variable, the initial data shuffling affects the composition of the sets and leads to the non-zero standard deviations for all the models.

In the size-based splits, ascending is more challenging than descending, since a model trained on large molecules also has a notion of atoms in smaller molecules. In principle, property-based splits are equally challenging as ascending or descending, but due to asymmetry in the data distributions, ascending seems to result in higher test MAEs for all models.

Dataset (property, units)	Atom-mapping regime	CHEMPROP	SLATM _d +KRR	INREACT	EQUIREACT
<i>Scaffold splits</i>					
GDB7-22-TS (ΔE^\ddagger , kcal/mol)	True	7.1 \pm 0.6	—	7.8 \pm 0.7	7.8 \pm 0.8
	RXNMapper	8.7 \pm 0.8	—	9.2 \pm 0.8	9.1 \pm 0.8
	None	12.9 \pm 0.6	11.0 \pm 1.0	10.1 \pm 0.9	10.0 \pm 0.9
Cyclo-23-TS (ΔG^\ddagger , kcal/mol)	True	2.92 \pm 0.24	—	2.79 \pm 0.18	2.72 \pm 0.18
	RXNMapper	2.92 \pm 0.23	—	2.77 \pm 0.22	2.71 \pm 0.23
	None	3.1 \pm 0.3	2.97 \pm 0.22	2.76 \pm 0.22	2.72 \pm 0.19
Proparg-21-TS (ΔE^\ddagger , kcal/mol)	True	1.64 \pm 0.21	—	0.44 \pm 0.11	0.40 \pm 0.08
	None	1.64 \pm 0.19	0.36 \pm 0.05	0.45 \pm 0.10	0.41 \pm 0.09
<i>Property-based splits (ascending)</i>					
GDB7-22-TS (ΔE^\ddagger , kcal/mol)	True	29.0 \pm 0.9	—	30.9 \pm 0.6	30.9 \pm 0.5
	RXNMapper	31.7 \pm 0.9	—	33.0 \pm 0.4	32.2 \pm 0.6
	None	36.0 \pm 0.4	34.80	35.3 \pm 0.3	35.3 \pm 0.4
Cyclo-23-TS (ΔG^\ddagger , kcal/mol)	True	11.7 \pm 0.3	—	9.0 \pm 0.6	9.3 \pm 0.4
	RXNMapper	12.1 \pm 0.3	—	8.8 \pm 0.7	8.8 \pm 0.6
	None	11.9 \pm 0.3	12.14	9.5 \pm 0.3	9.6 \pm 0.4
Proparg-21-TS (ΔE^\ddagger , kcal/mol)	True	5.10 \pm 0.12	—	4.31 \pm 0.15	4.08 \pm 0.11
	None	5.09 \pm 0.13	5.83	4.53 \pm 0.16	4.33 \pm 0.14
<i>Property-based splits (descending)</i>					
GDB7-22-TS (ΔE^\ddagger , kcal/mol)	True	24.0 \pm 1.1	—	24.9 \pm 0.9	25.0 \pm 0.7
	RXNMapper	25.7 \pm 0.7	—	26.8 \pm 0.9	26.4 \pm 0.4
	None	30.3 \pm 0.5	31.08	30.6 \pm 0.6	31.0 \pm 0.3
Cyclo-23-TS (ΔG^\ddagger , kcal/mol)	True	6.1 \pm 0.4	—	5.03 \pm 0.28	4.8 \pm 0.5
	RXNMapper	5.9 \pm 0.8	—	5.2 \pm 0.4	4.6 \pm 0.5
	None	6.22 \pm 0.30	6.46	5.18 \pm 0.17	5.07 \pm 0.28
Proparg-21-TS (ΔE^\ddagger , kcal/mol)	True	3.33 \pm 0.20	—	1.58 \pm 0.12	1.69 \pm 0.20
	None	3.28 \pm 0.23	2.02	1.70 \pm 0.11	2.13 \pm 0.27
<i>Size-based splits (ascending)</i>					
GDB7-22-TS (ΔE^\ddagger , kcal/mol)	True	5.62 \pm 0.20	—	6.41 \pm 0.25	6.36 \pm 0.24
	RXNMapper	6.97 \pm 0.25	—	7.52 \pm 0.19	7.55 \pm 0.28
	None	10.39 \pm 0.14	8.06 \pm 0.16	8.10 \pm 0.22	8.11 \pm 0.23
Cyclo-23-TS (ΔG^\ddagger , kcal/mol)	True	4.57 \pm 0.15	—	3.86 \pm 0.13	3.86 \pm 0.11
	RXNMapper	4.68 \pm 0.13	—	3.91 \pm 0.13	3.89 \pm 0.21
	None	4.57 \pm 0.11	4.79 \pm 0.03	3.96 \pm 0.13	3.96 \pm 0.16
Proparg-21-TS (ΔE^\ddagger , kcal/mol)	True	1.537 \pm 0.023	—	0.52 \pm 0.07	0.48 \pm 0.05
	None	1.538 \pm 0.026	0.504 \pm 0.021	0.63 \pm 0.06	0.55 \pm 0.05
<i>Size-based splits (descending)</i>					
GDB7-22-TS (ΔE^\ddagger , kcal/mol)	True	3.25 \pm 0.05	—	3.78 \pm 0.14	3.74 \pm 0.10
	RXNMapper	4.61 \pm 0.15	—	4.75 \pm 0.12	4.74 \pm 0.13
	None	8.36 \pm 0.22	4.85 \pm 0.07	4.90 \pm 0.11	4.90 \pm 0.11
Cyclo-23-TS (ΔG^\ddagger , kcal/mol)	True	2.85 \pm 0.08	—	2.74 \pm 0.10	2.72 \pm 0.06
	RXNMapper	2.88 \pm 0.06	—	2.77 \pm 0.09	2.72 \pm 0.07
	None	2.85 \pm 0.07	2.80 \pm 0.03	2.85 \pm 0.07	2.76 \pm 0.09
Proparg-21-TS (ΔE^\ddagger , kcal/mol)	True	1.30 \pm 0.04	—	0.278 \pm 0.021	0.263 \pm 0.023
	None	1.30 \pm 0.04	0.307 \pm 0.011	0.236 \pm 0.029	0.226 \pm 0.028

TABLE S5. Performance as measured in mean absolute errors (MAEs) of predictions of 3DREACT (INREACT and EQUIREACT) vs. CHEMPROP and SLATM_d. MAEs are averaged over 10 folds of 80/10/10 splits (training/validation/test) and reported together with standard deviations across folds. Lowest errors are highlighted in bold, if there are statistically meaningful differences between models in each regime/dataset/split type tested.

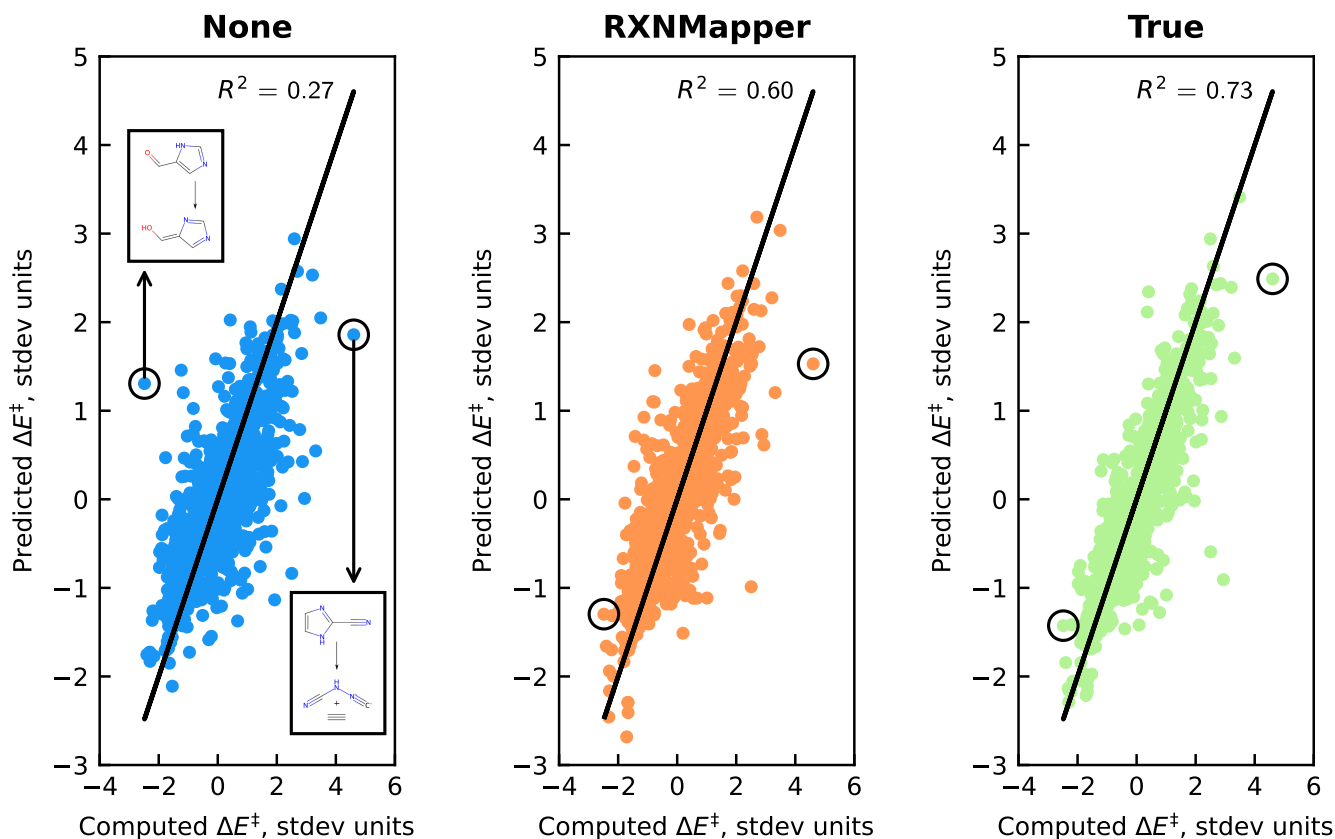


FIG. S3. Correlation plots of predicted with 3DREACT (INREACT) ΔE^\ddagger values *vs.* true (computed) labels for the first reactant-based scaffold split on the GDB7-22-TS dataset. The same test reactions are highlighted in each subplot.

S6. CORRELATION PLOTS FOR THE GDB7-22-TS DATASET

Figure S3 illustrates that for the same scaffold split, from “None” to “RXNMapper” to “True” the coefficient of determination (R^2) increases and outliers successively move closer to the $y = x$ line.

S7. PERFORMANCE WITH AND WITHOUT EXPLICIT HYDROGEN ATOMS

The results presented in the main text were for models built from molecular graphs constructed without explicit inclusion of hydrogen atoms as nodes. The performance for models including H-nodes is shown in Table S6.

For the GDB7-22-TS dataset, the best-performing model in the “True” regime (CHEMPROP) is with explicit Hs. Since this set includes H_2 -abstraction reactions, the explicit inclusion of hydrogen in combination with the reaction mechanism in the form of atom-mapping is particularly informative. Interestingly, 3DREACT “True” and “None” does not suffer when removing H atoms. In the “RXNMapper” regime, the inclusion of H-nodes increases the errors especially for CHEMPROP. The atom-mapping provided by RXNMAPPER is inferred as a consequence of a related task: predicting randomly masked parts of a reaction sequence (reaction SMILES).^{S8} Since there are few H atoms in reaction SMILES strings (typically they are implicit), it is natural that RXNMAPPER struggles to map H atoms in reactions.

For the Cyclo-23-TS and Proparg-21-TS datasets, no models benefit from the inclusion of explicit Hs in any regime. Since larger molecules participate in these reactions which never consist purely of H_2 -abstraction, the reactions are well-described without an explicit description of H atoms. The cost of the message passing increases considerably when including H-nodes, and 3DREACT’s performance is not strongly correlated with their inclusion. This coupled with the fact that atom-mapping tools usually do not map hydrogens, as well as the fact that most atom-mapped reaction SMILES have maps only for heavy atoms, resulted in the decision that we use the models without explicit

H-nodes in CHEMPROP and 3DREACT.

Dataset (property, units)	H mode	Atom mapping regime					
		True		RXNMapper		None	
		CHEMPROP	3DREACT _M	CHEMPROP	3DREACT _M	CHEMPROP	3DREACT _S
GDB7-22-TS (ΔE^\ddagger , kcal/mol)	with	4.12 ± 0.13	4.90 ± 0.16	6.36 ± 0.09	6.24 ± 0.21	8.87 ± 0.28	6.54 ± 0.25
	w/o	4.35 ± 0.15	4.93 ± 0.18	5.69 ± 0.17	6.03 ± 0.26	9.04 ± 0.21	6.56 ± 0.26
Cyclo-23-TS (ΔG^\ddagger , kcal/mol)	with	—	2.33 ± 0.07	2.79 ± 0.12	2.37 ± 0.07	2.76 ± 0.10	2.38 ± 0.08
	w/o	2.69 ± 0.10	2.39 ± 0.08	2.71 ± 0.07	2.37 ± 0.07	2.71 ± 0.12	2.39 ± 0.05
Proparg-21-TS (ΔE^\ddagger , kcal/mol)	with	1.55 ± 0.16	0.38 ± 0.07	—	—	1.54 ± 0.14	0.37 ± 0.05
	w/o	1.53 ± 0.14	0.33 ± 0.07	—	—	1.56 ± 0.16	0.34 ± 0.06

TABLE S6. Performance of 3DREACT (INREACT) with explicit hydrogens as nodes in the graphs (H mode “with”) and without (H mode “w/o”, as in the main text). Cyclo-23-TS “True” with Hs is missing because the dataset provides atom maps for heavy atoms only, while 3DREACT does not suffer from that since it uses atom-mapped xyz files (see Section 5.1). MAEs are averaged over 10 folds of 80/10/10 splits (training/validation/test) and reported together with standard deviations across folds. Lowest errors, if statistically relevant, in each dataset/mapping regime are highlighted in bold.

Figure S4 illustrates the performance of 3DREACT “True” trained with explicit H-nodes. Compared to the model trained without explicit H-nodes (Figure 7 in the main text), the error distribution in the different reaction types is more uniform, since the GDB7-22-TS dataset consists of many reactions involving breaking and forming H–X bonds, which are better captured using a model with explicit H atoms. Nevertheless, 3DREACT without explicit Hs already performs well across the different reaction classes, in exchange for faster message passing.

Table S7 shows the performance of SLATM_d+KRR with SLATM features constructed in three ways: with Hs (“with”), with H features removed after building the representation (“w/o after”) and H atoms removed before building the representation (“w/o before”). The first variation is the standard construction of SLATM features.^{S9} The second variation is the closest possible version to “implicit” H regimes of CHEMPROP and 3DREACT since the H-only features (H–H and X–H–Y bins) are removed. Nevertheless, other H-containing bins, *e.g.* C–H or C–C–H, are still incorporated. The last version removes H atoms completely from the system. For the GDB7-22-TS set, which is dependent on an accurate description of X–H bonds, errors increase systematically on the removal of H information. The same is seen to a lesser extent in the Cyclo-23-TS set. For the Proparg-21-TS, X–H bond changes have a minimal impact on the description of the reactions. SLATM_d is run with explicit H atoms by default, since the representation is constructed from the xyz file directly without use of SMILES strings. Regardless of whether H atoms are in the SMILES strings, they are always present in the xyz file and therefore excluding H is nonsensical for SLATM.

H mode	GDB7-22-TS (ΔE^\ddagger , kcal/mol)	Cyclo-23-TS (ΔG^\ddagger , kcal/mol)	Proparg-21-TS (ΔE^\ddagger , kcal/mol)
with	6.89 ± 0.20	2.65 ± 0.08	0.33 ± 0.04
w/o after	7.11 ± 0.20	2.69 ± 0.08	0.33 ± 0.04
w/o before	8.04 ± 0.22	2.82 ± 0.09	0.34 ± 0.04

TABLE S7. Performance of SLATM_d+KRR with hydrogens in the representation (H mode “with”, as in the main text), with hydrogens excluded after computing the representation (H mode “w/o after”), and with hydrogens excluded before computing the representation (H mode “w/o before”). MAEs are averaged over 10 folds of 80/10/10 splits (training/validation/test) and reported together with standard deviations across folds.

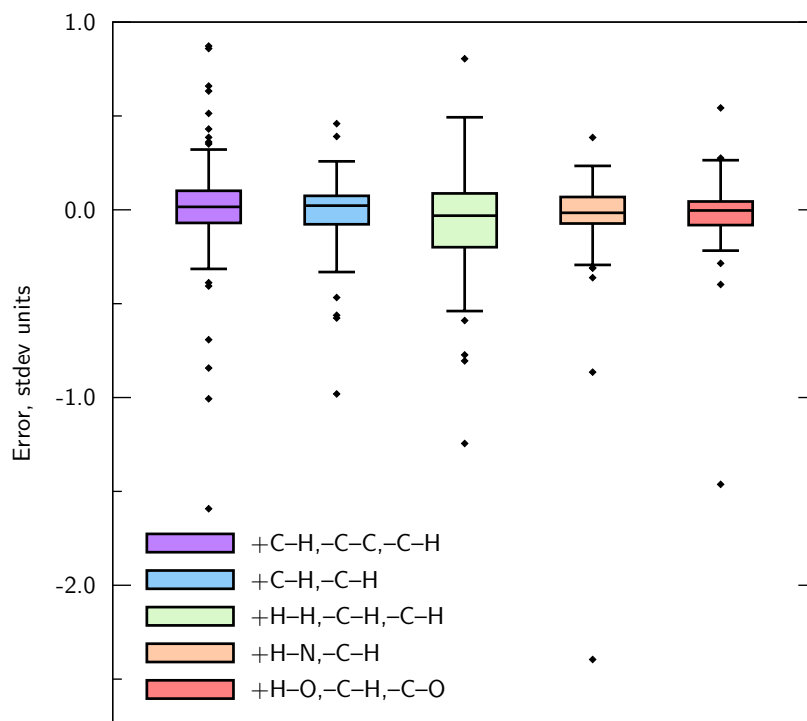


FIG. S4. Box plots illustrating how 3DREACT (INREACT_M “True”) performs for the most common reaction types in the GDB7-22-TS set, when using explicit H nodes in the graphs. The boxes range from the first to the third quartile of the datapoints. The whiskers limit 90% of the datapoints and the individual points illustrate outliers. The points correspond to the test set of the first random split. The errors are given in the target standard deviation (stdev) units (21.8 kcal/mol).

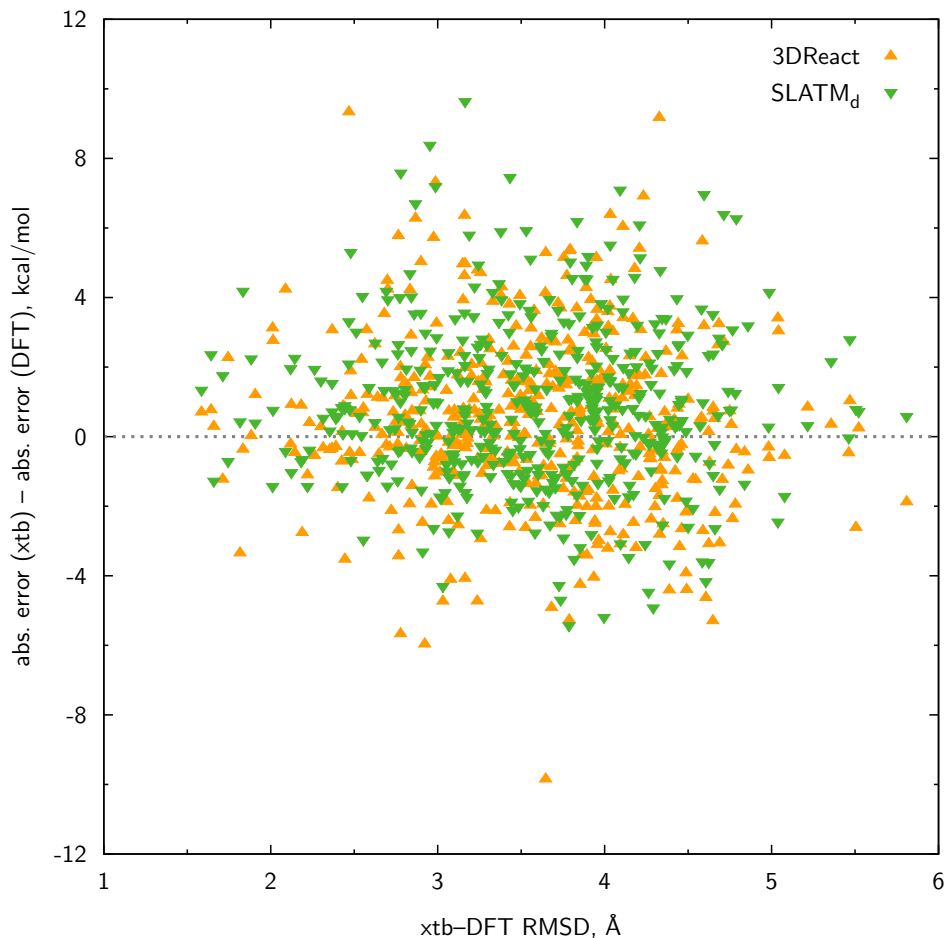


FIG. S5. Difference between absolute prediction errors using lower-quality GFN2-xTB^{S12} (xtb) and provided (DFT) geometries *vs.* root-mean-square distance (RMSD) between said geometries on the Cyclo-23-TS set for 3DReact (INREACT_M “True”) and SLATM_d+KRR.

S8. GEOMETRY SENSITIVITY FOR THE CYCLO-23-TS DATASET

Figure S5 shows the difference between absolute errors of models trained using GFN2-xTB (xtb) and DFT geometries for both 3DReact and SLATM_d+KRR *vs.* the root-mean-square distance (RMSD) between the xtb and DFT geometries (as a measure of the agreement of the structures). There is no noticeable trend for either model. This is likely because a model trained on lower quality geometries then struggles universally to predict barriers for lower quality geometries, rather than resulting in larger errors for higher RMSD molecules.

RMSD^{S10} is computed as $\sqrt{\text{RMSD}_{\text{reactant}_1}^2 + \text{RMSD}_{\text{reactant}_2}^2 + \text{RMSD}_{\text{product}}^2}$ using the `rmsd`^{S11} python package.

REFERENCES

- ^{S1}G. Landrum, P. Tosco, B. Kelley, Ric, Sriniker, D. Cosgrove, Gedeck, R. Vianello, NadineSchneider, E. Kawashima, D. N, G. Jones, A. Dalke, B. Cole, M. Swain, S. Turk, AlexanderSavelyev, A. Vaucher, M. Wójcikowski, Ichiru Take, D. Probst, K. Ujihara, V. F. Scalfani, G. Godin, A. Pahl, Francois Berenger, JLVarjo, R. Walker, Jasondbiggs, and Strets123, rdkit/rdkit: 2023_03_1 (q1 2023) release (2023).
- ^{S2}G. Corso, H. Stärk, B. Jing, R. Barzilay, and T. Jaakkola, arXiv preprint , arXiv:2210.01776 (2023).
- ^{S3}<https://docs.e3nn.org/en/stable/guide/irreps.html>.
- ^{S4}M. Geiger, T. Smidt, A. M., B. K. Miller, W. Boomsma, B. Dice, K. Lapchevskyi, M. Weiler, M. Tyszkiewicz, M. Uhrin, S. Bätzner, D. Madiseti, J. Frellsen, N. Jung, S. Sanborn, jkh, M. Wen, J. Rackers, M. Rød, and M. Bailey, e3nn/e3nn: 2022-12-12 (2022).
- ^{S5}A. Vaswani, N. Shazeer, N. Parmar, J. Uszkoreit, L. Jones, A. N. Gomez, Ł. Kaiser, and I. Polosukhin, Adv. Neural Inf. Process. Syst. **30**, 5998 (2017).
- ^{S6}A. Paszke, S. Gross, F. Massa, A. Lerer, J. Bradbury, G. Chanan, T. Killeen, Z. Lin, N. Gimelshein, L. Antiga, A. Desmaison, A. Kopf, E. Yang, Z. DeVito, M. Raison, A. Tejani, S. Chilamkurthy, B. Steiner, L. Fang, J. Bai, and S. Chintala, Adv. Neural Inf. Process. Syst. **32**, 8026 (2019).
- ^{S7}K. Spiekermann, L. Pattanaik, and W. H. Green, Sci. Data **9**, 417 (2022).
- ^{S8}P. Schwaller, B. Hoover, J.-L. Reymond, H. Strobelt, and T. Laino, Sci. Adv. **7**, eabe4166 (2021).
- ^{S9}B. Huang and O. A. von Lilienfeld, Nat. Chem. **12**, 945 (2020).
- ^{S10}W. Kabsch, Acta Crystallogr. A **32**, 922 (1976).
- ^{S11}J. C. Kromann, Calculate root-mean-square deviation (RMSD) of two molecules using rotation, <https://github.com/charnley/rmsd/releases/tag/rmsd-1.5.1> (2023).
- ^{S12}C. Bannwarth, S. Ehlert, and S. Grimme, J. Chem. Theory Comput. **15**, 1652 (2019).